

# Detonations in white dwarf dynamical interactions

G. Aznar-Siguán<sup>1,2</sup>, E. García-Berro<sup>1,2</sup>, P. Lorén-Aguilar<sup>3</sup>, J. José<sup>4,2</sup> and J. Isern<sup>5,2</sup>

<sup>1</sup>*Departament de Física Aplicada, Universitat Politècnica de Catalunya, c/Esteve Terrades 5, 08860 Castelldefels, Spain*

<sup>2</sup>*Institute for Space Studies of Catalonia, c/Gran Capità 2–4, Edif. Nexus 104, 08034 Barcelona, Spain*

<sup>3</sup>*School of Physics, University of Exeter, Stocker Road, Exeter, UK EX4 4QL, United Kingdom*

<sup>4</sup>*Departament de Física i Enginyeria Nuclear, Universitat Politècnica de Catalunya, c/Comte d’Urgell 187, 08036 Barcelona, Spain*

<sup>5</sup>*Institut de Ciències de l’Espai, CSIC, Campus UAB, Facultat de Ciències, Torre C-5, 08193 Bellaterra, Spain*

March 9, 2018

## ABSTRACT

In old, dense stellar systems collisions of white dwarfs are a rather frequent phenomenon. Here we present the results of a comprehensive set of Smoothed Particle Hydrodynamics simulations of close encounters of white dwarfs aimed to explore the outcome of the interaction and the nature of the final remnants for different initial conditions. Depending on the initial conditions and the white dwarf masses, three different outcomes are possible. Specifically, the outcome of the interaction can be either a direct or a lateral collision or the interaction can result in the formation of an eccentric binary system. In those cases in which a collision occurs, the infalling material is compressed and heated such that the physical conditions for a detonation may be reached during the most violent phases of the merger. While we find that detonations occur in a significant number of our simulations, in some of them the temperature increase in the shocked region rapidly lifts degeneracy, leading to the quenching of the burning. We thus characterize under which circumstances a detonation is likely to occur as a result of the impact of the disrupted star on the surface of the more massive white dwarf. Finally, we also study which interactions result in bound systems, and in which ones the more massive white dwarf is also disrupted as a consequence of the dynamical interaction. The sizable number of simulations performed in this work allows to find how the outcome of the interaction depends on the distance at closest approach, and on the masses of the colliding white dwarfs, and which is the chemical pattern of the nucleary processed material. Finally, we also discuss the influence of the masses and core chemical compositions of the interacting white dwarfs and the different kinds of impact in the properties of the remnants.

**Key words:** Hydrodynamics — nuclear reactions, nucleosynthesis, abundances — (stars:) white dwarfs — (stars:) supernovae: general — globular clusters: general.

## 1 INTRODUCTION

In globular clusters, the density of stars is roughly a million times that of our Solar System’s environs. In such dense stellar systems stellar collisions are rather frequent (Hills & Day 1976). Actually, it has been predicted that up to 10% of the stars in the core of typical globular clusters have undergone a collision at some point during the lifetime of the cluster (Davies 2002). Also, galactic nuclei which harbor massive black holes, like that of our own Galaxy, have stellar densities at least as large as those found in the center of the densest globular clusters. Moreover, in these environments the frequency of stellar collisions is strongly enhanced, since due to strong attraction of their central black holes, stars have much larger velocities.

In these very dense stellar systems the most probable

collisions are those in which at least one of the colliding stars has a large cross-section — a red giant or an AGB star — and those in which at least one of the stars is common (Shara & Regev 1986). Since white dwarfs are the most usual end-point of stellar evolution, and because both globular clusters and galactic nuclei are rather old, these stellar systems contain many degenerate stars. Therefore, collisions in which one of the colliding stars is a white dwarf should be rather common (Lorén-Aguilar et al. 2010). Additionally, it has been recently shown that close encounters of two white dwarfs could be more frequent than previously thought (Katz & Dong 2012).

Recently, the study of the collisions of two white dwarfs has received considerable interest, since it has been shown that, under certain circumstances, the result of such interactions could be a Type Ia supernova outburst (Raskin et al.

2009, 2010; Rosswog et al. 2009). Moreover, it has also been suggested that such processes could not only lead to Type Ia supernova explosions, but also to the formation of magnetars (King et al. 2001), and could also be at the origin of high-field magnetic white dwarfs (García-Berro et al. 2012). Additionally, this is a suggestive scenario which could also explain some of the characteristics of soft gamma-ray repeaters and of anomalous X-ray pulsars (Malheiro et al. 2012). It is also interesting to note that dynamical interactions in globular clusters can form double white dwarfs with non-zero eccentricities. These systems are powerful sources of gravitational waves (Willems et al. 2007), which could be eventually detected by spaceborne observatories (Lorén-Aguilar et al. 2005). Finally, another important property of the collision of white dwarfs is that the temperatures achieved in direct collisions are substantially high, and consequently some of the nuclear processed material ejected during the interaction could pollute the surrounding environment (Lorén-Aguilar et al. 2010).

All in all, it is clear that for multiple reasons the collision of two white dwarfs is a subject that deserves to be studied in detail. However, there are very few simulations of this phenomenon. In fact, the small number of simulations of white dwarf collisions is noticeable when compared to the number of simulations in which two white dwarfs belonging to a binary system merge. Specifically, the first simulations of colliding white dwarfs (Benz et al. 1989) were done using a Smoothed Particle Hydrodynamics (SPH) method, but employing a rather small number of particles in the calculations, a consequence of the severe computational limitations. Other recent calculations (Rosswog et al. 2009) also employed SPH techniques, but due to the large parameter space to be studied, the calculations were mostly restricted to head-on collisions, this time using a large number of particles. The reason for this choice was that these simulations were primarily aimed at obtaining a thermonuclear explosion, and it was foreseen that very high temperatures were most likely to be obtained in these kind of interactions. This was also the aim of subsequent calculations (Raskin et al. 2009, 2010), which independently confirmed the results of Rosswog et al. (2009) using an independent SPH code. Finally, the collisions of two white dwarfs have also been studied recently using the Eulerian adaptive grid code FLASH (Hawley et al. 2012). However, these authors only computed zero impact parameter collisions for two equal-mass white dwarfs, a  $0.64 M_{\odot} + 0.64 M_{\odot}$  pair and a  $0.81 M_{\odot} + 0.81 M_{\odot}$  system. As in most of the previous studies of this kind, the primary goal of this work was again to study an independent channel for producing Type Ia supernovae.

In summary, most authors have studied the collision of two white dwarfs with fixed masses, and have varied the total energy and angular momentum of the colliding white dwarfs, while little attention has been paid up to now to study the effects of the masses of the interacting stars. This was also the approach adopted by Lorén-Aguilar et al. (2010), where the masses of the intervening white dwarfs ( $0.8 M_{\odot}$  and  $0.6 M_{\odot}$ ) were kept fixed, while their initial relative velocity and distance were varied. They found that the outcome of the interaction could be either a direct collision, a lateral one, or could be the formation of an eccentric binary system. Nevertheless, the outcome of the dynamical interaction

depends on the masses (and on the core chemical composition) of the interacting white dwarfs. Thus, a comprehensive study of the interactions of two white dwarfs covering a broad range of masses and initial conditions is still lacking. The present work aims precisely at filling this gap.

Our paper is organized as follows. In Sect. 2 the input physics and the method of calculation used in the simulations described here are briefly explained. We pay special attention to the numerical technique employed in our calculations, the so-called SPH method, and to our current implementation of such technique. Sect. 3 is devoted to present the initial conditions used in this work. It follows Sect. 4, where the outcomes of the collisions and close encounters are presented and analyzed. In Sect. 5 we present the most significant features of the extensive set of simulations performed so far. Finally, in Sect. 6 we summarize our main findings, we discuss their significance and we draw our conclusions.

## 2 INPUT PHYSICS AND METHOD OF CALCULATION

As mentioned earlier, the hydrodynamic evolution of the interacting white dwarfs has been followed using a SPH code. SPH is a Lagrangian particle numerical method. It was first proposed by Lucy (1977) and, independently, by Gingold & Monaghan (1977). The basic principle of SPH methods consists in discretizing the fluid in a set of elements, referred to as particles. These particles have a spatial dimension (known as the “smoothing length”,  $h$ ), over which their properties are smoothed using a kernel. In the following we explain the main features that characterize our SPH code.

Our SPH code is fully parallel, and allows to run simulations with a large number of particles in a reasonable time. We use the standard cubic spline kernel of Monaghan & Lattanzio (1985). The gravitational interaction is also softened using this kernel (Hernquist & Katz 1989). The search of neighbors and the evaluation of the gravitational forces are performed using an octree (Barnes & Hut 1986). This is a tree method which allows to directly calculate the force in the gravitational  $N$ -body problem. The computational load of this method grows only as  $N \log N$ . To determine the smoothing length of each particle we use a standard prescription:

$$h_i = \eta \left( \frac{m_i}{\rho_i} \right)^{1/3} \quad (1)$$

We also consider the effect of the gradient of the smoothing length on the SPH equations, which is given by:

$$\Omega_i = \left( 1 - \frac{\partial h_i}{\partial \rho_i} \sum_j m_j \frac{\partial W_{ij}(h_i)}{\partial h_i} \right). \quad (2)$$

To deal numerically with shocks, where on the macroscopic scales of a simulation the very steep gradients appear as discontinuous, artificial viscosity is usually added to the SPH equations. The SPH code employed in the simulations uses a prescription for the artificial viscosity based in

Riemann-solvers (Monaghan 1997):

$$\Pi_{ij} = -\alpha \frac{v_{ij}^{\text{sig}}}{\bar{\rho}_{ij}} \mathbf{v}_{ij} \cdot \hat{\mathbf{e}}_{ij} \quad (3)$$

where the signal velocity is taken as  $v_{ij}^{\text{sig}} = \bar{c}_{ij} - \min\{0, \mathbf{v}_{ij} \cdot \hat{\mathbf{e}}_{ij}\}$  and  $\bar{c}_{ij} = (c_{si} + c_{sj})/2$  is the averaged sound speed. The other variables have their usual meaning:  $\bar{\rho}_{ij} = (\rho_i + \rho_j)/2$ ,  $\mathbf{v}_{ij} = \mathbf{v}_i - \mathbf{v}_j$ ,  $\hat{\mathbf{e}}_{ij} = \mathbf{r}_{ij}/|\mathbf{r}_{ij}|$ ,  $\mathbf{r}_{ij} = \mathbf{r}_i - \mathbf{r}_j$  and  $\alpha$  is an adjustable parameter. Normally,  $\alpha = 0.5$  yields good results. Additionally, to suppress artificial viscosity forces in pure shear flows the viscosity switch of Balsara (1995) is also used:

$$f_i = \frac{|\nabla \cdot \mathbf{v}|_i}{|\nabla \cdot \mathbf{v}|_i + |\nabla \times \mathbf{v}|_i + 10^{-4} c_i/h_i}$$

In this way the dissipative terms are largely reduced in most parts of the fluid and are only used where they are really necessary to resolve a shock, if present.

Within this approach, the SPH equations for the momentum and energy conservation read respectively:

$$\begin{aligned} \frac{d\mathbf{v}_i}{dt} &= - \sum_j m_j \left[ \frac{P_i}{\rho_i^2 \Omega_i} F_{ij}(h_i) + \frac{P_j}{\rho_j^2 \Omega_j} F_{ij}(h_j) \right. \\ &\quad \left. + \bar{f}_{ij} \frac{\Pi_{ij}}{2} \left( \frac{1}{\Omega_i} F_{ij}(h_i) + \frac{1}{\Omega_j} F_{ij}(h_j) \right) \right] \mathbf{r}_{ij} - \nabla \Phi_i \quad (4) \end{aligned}$$

$$\frac{du_i}{dt} = \frac{1}{\Omega_i} \sum_j m_j F_{ij}(h_i) \left( \frac{P_i}{\rho_i^2} + \frac{\Pi_{ij}}{2} \bar{f}_{ij} \right) \mathbf{v}_{ij} \cdot \mathbf{r}_{ij} + \varepsilon_i \quad (5)$$

where we have used a function  $F(r/h)$  such that the gradient of the kernel is  $\nabla_i W_{ij}(h) = F_{ij}(h) \mathbf{r}_{ij}$ . We also took into account the energy released by nuclear reactions,  $\varepsilon_i$ .

We found that it is sometimes advisable to use a different formulation of the equation of energy conservation (Guerrero et al. 2004; Lorén-Aguilar et al. 2005, 2009). Accordingly, for each timestep the variation of the internal energy is computed using Eq. (5) and simultaneously the variation of temperature is computed using:

$$\begin{aligned} \frac{dT_i}{dt} &= \frac{1}{\Omega_i} \sum_{j=1}^N \frac{m_j}{C_{vi}} \left( \frac{T_i}{\rho_i^2} \left[ \left( \frac{\partial P}{\partial T} \right)_{\rho_i} \right] + \frac{\Pi_{ij}}{2} \bar{f}_{ij} \right) \\ &\quad \mathbf{v}_{ij} \cdot \mathbf{r}_{ij} F_{ij}(h_i) + \frac{\varepsilon_i}{C_{vi}} \quad (6) \end{aligned}$$

where  $C_v$  is the specific heat. In order to avoid errors made when computing the temperature from the internal energy in degenerate regions, we compare the temperatures obtained when using Eqs. (5) and (6). If the difference between both values is larger than 5%, we consider the temperature obtained using Eq. (6). Otherwise, we follow the temperature evolution of the SPH particles using Eq. (5). Using this prescription energy is best conserved.

Regarding the integration method, a predictor-corrector numerical scheme with variable timestep (Serna et al. 1996), which turns out to be quite accurate, is used. The sequence initiates by predicting variable values (denoted by primes) at  $t_{n+1}$  according to

$$\begin{aligned} \mathbf{r}'_{n+1} &= \mathbf{r}_n + \mathbf{v}_n \Delta t_n + \mathbf{a}'_n (\Delta t_n)^2 / 2 \\ \mathbf{v}'_{n+1} &= \mathbf{v}_n + \mathbf{a}'_n \Delta t_n \\ \mathbf{u}'_{n+1} &= \mathbf{u}_n + \dot{\mathbf{u}}'_n \Delta t_n \\ \mathbf{T}'_{n+1} &= \mathbf{T}_n + \dot{\mathbf{T}}'_n \Delta t_n \end{aligned}$$

The above predicted quantities are then used to compute  $\mathbf{a}'_{n+1}$ ,  $\dot{\mathbf{u}}'_{n+1}$  and  $\dot{\mathbf{T}}'_{n+1}$  at  $\mathbf{r}_{n+1}'$  using Eqs. (4), (5) and (6). The predicted quantities are then used to correct the positions, velocities, thermal energies and temperatures:

$$\begin{aligned} \mathbf{r}_{n+1} &= \mathbf{r}'_{n+1} + A(\mathbf{a}'_{n+1} - \mathbf{a}'_n) (\Delta t_n)^2 / 2 \\ \mathbf{v}_{n+1} &= \mathbf{v}'_{n+1} + B(\mathbf{a}'_{n+1} - \mathbf{a}'_n) \Delta t_n \\ \mathbf{u}_{n+1} &= \mathbf{u}'_{n+1} + C(\dot{\mathbf{u}}'_{n+1} - \dot{\mathbf{u}}'_n) \Delta t_n \\ \mathbf{T}_{n+1} &= \mathbf{T}'_{n+1} + C(\dot{\mathbf{T}}'_{n+1} - \dot{\mathbf{T}}'_n) \Delta t_n \end{aligned}$$

where  $B = 1/2$  is required to obtain accurate velocities to second order and the values of  $A$  and  $C$  are somewhat arbitrary. We adopt  $A = 1/3$  and  $C = 1/2$ . Finally, timesteps ( $\Delta t_n$ ) are determined comparing the local sound velocity with the local acceleration and imposing that none of the SPH particles travels a distance larger than its corresponding smoothing length. Also the change in the internal energy is taken into account to restrict the timesteps. In particular, timesteps are computed in the following way:

$$\Delta t^{n+1} = \min_i \Delta t_i^{n+1}$$

$$\Delta t_i^{n+1} = \min \left( f_h, \sqrt{\frac{h_i^n}{|\mathbf{a}_i^n|}}, f_h \frac{h_i^n}{v_i^{\text{sig},n}}, f_u \Delta t^n \frac{u_i^{n-1}}{u_i^n - u_i^{n-1}} \right)$$

with  $f_h = 0.5$  and  $f_u = 0.3$ . Adopting all these prescriptions, energy is conserved at the level of 1%, and angular momentum at the level of  $10^{-3}\%$  in all simulations.

The thermodynamical properties of matter are computed using the Helmholtz equation of state (Timmes & Swesty 2000). The nuclear network adopted here incorporates 14 nuclei: He, C, O, Ne, Mg, Si, S, Ar, Ca, Ti, Cr, Fe, Ni and Zn. The reactions considered are captures of  $\alpha$  particles, and the associated back reactions (photo-disintegrations), the fusion of two C nuclei and the reaction between C and O nuclei. All the thermonuclear reaction rates are taken from the REACLIB data base (Cyburt et al. 2010). The screening factors adopted in this work are those of Itoh et al. (1979). The nuclear energy release is computed independently of the dynamical evolution with much shorter timesteps, assuming that the dynamical variables do not change during these time steps. Nevertheless, when photo-disintegrations occur the temperatures and the specific heat are updated, following the procedure detailed in Raskin et al. (2010). Nuclear abundances are obtained by means of an iterative pseudo-Gaussian elimination technique based on a two-step linearization procedure (Wagoner 1969).

### 3 INITIAL CONDITIONS

We have relaxed five different white dwarf models with masses  $M_1 = 0.4 M_\odot, 0.6 M_\odot, 0.8 M_\odot, 1.0 M_\odot$  and  $1.2 M_\odot$ . The chemical composition of all white dwarfs is a mixture of

**Table 1.** Kinematical properties of the simulations reported here involving a  $0.8 M_{\odot}$  white dwarf.

Run	$M_1 + M_2$ ( $M_{\odot}$ )	Outcome	Detonation	Ejection	$E$ ( $10^{48}$ erg)	$L$ ( $10^{50}$ erg s $^{-1}$ )	$r_{\max}$ ( $R_{\odot}$ )	$r_{\min}$ ( $R_{\odot}$ )	$\varepsilon$	$\beta$
$v_{\text{ini}} = 75$ km/s		$\Delta y = 0.4 R_{\odot}$								
1	0.8+0.6	DC	Yes	No	-4.12	2.80	$4.48 \times 10^{-1}$	$6.72 \times 10^{-3}$	0.970	2.83
2	0.8+0.8	DC	Yes	No	-5.49	3.28	$4.49 \times 10^{-1}$	$5.88 \times 10^{-3}$	0.974	3.06
3	1.0+0.8	DC	Yes	2	-6.88	3.64	$4.49 \times 10^{-1}$	$5.21 \times 10^{-3}$	0.977	3.07
4	1.2+0.8	DC	Yes	1	-8.26	3.93	$4.48 \times 10^{-1}$	$4.70 \times 10^{-3}$	0.980	2.98
$v_{\text{ini}} = 100$ km/s		$\Delta y = 0.3 R_{\odot}$								
5	0.8+0.6	DC	Yes	No	-5.05	2.81	$3.64 \times 10^{-1}$	$6.76 \times 10^{-3}$	0.964	2.81
6	0.8+0.8	DC	Yes	No	-6.76	3.28	$3.63 \times 10^{-1}$	$5.90 \times 10^{-3}$	0.968	3.05
7	1.0+0.8	DC	Yes	2	-8.47	3.64	$3.63 \times 10^{-1}$	$5.23 \times 10^{-3}$	0.972	3.06
8	1.2+0.8	DC	Yes	1	-10.1	3.93	$3.63 \times 10^{-1}$	$4.71 \times 10^{-3}$	0.974	2.97
$v_{\text{ini}} = 100$ km/s		$\Delta y = 0.4 R_{\odot}$								
9	0.8+0.6	LC	Yes	No	-4.06	3.74	$4.49 \times 10^{-1}$	$1.21 \times 10^{-2}$	0.948	1.57
10	0.8+0.8	LC	Yes	No	-5.42	4.37	$4.50 \times 10^{-1}$	$1.05 \times 10^{-2}$	0.954	1.71
11	1.0+0.8	LC	Yes	No	-6.80	4.85	$4.50 \times 10^{-1}$	$9.35 \times 10^{-3}$	0.959	1.71
12	1.2+0.8	LC	Yes	No	-8.18	5.24	$4.49 \times 10^{-1}$	$8.42 \times 10^{-3}$	0.963	1.66
$v_{\text{ini}} = 150$ km/s		$\Delta y = 0.3 R_{\odot}$								
13	0.8+0.6	LC	No	No	-4.88	4.21	$3.68 \times 10^{-1}$	$1.56 \times 10^{-2}$	0.919	1.22
14	0.8+0.8	LC	Yes	No	-6.56	4.91	$3.67 \times 10^{-1}$	$1.35 \times 10^{-2}$	0.929	1.33
15	1.0+0.8	LC	Yes	No	-8.25	5.46	$3.66 \times 10^{-1}$	$1.20 \times 10^{-2}$	0.937	1.33
16	1.2+0.8	LC	Yes	No	-9.95	5.90	$3.66 \times 10^{-1}$	$1.08 \times 10^{-2}$	0.943	1.30
$v_{\text{ini}} = 150$ km/s		$\Delta y = 0.4 R_{\odot}$								
17	0.8+0.6	LC	No	No	-3.89	5.60	$4.53 \times 10^{-1}$	$2.81 \times 10^{-2}$	0.883	0.68
18	0.8+0.8	LC	No	No	-5.22	6.55	$4.54 \times 10^{-1}$	$2.45 \times 10^{-2}$	0.898	0.73
19	1.0+0.8	LC	No	No	-6.57	7.28	$4.53 \times 10^{-1}$	$2.16 \times 10^{-2}$	0.909	0.74
20	1.2+0.8	LC	Yes	No	-7.93	7.86	$4.52 \times 10^{-1}$	$1.94 \times 10^{-2}$	0.918	0.72
$v_{\text{ini}} = 200$ km/s		$\Delta y = 0.3 R_{\odot}$								
21	0.8+0.6	LC	No	No	-4.64	5.62	$3.75 \times 10^{-1}$	$2.86 \times 10^{-2}$	0.858	0.66
22	0.8+0.8	LC	No	No	-6.28	6.55	$3.73 \times 10^{-1}$	$2.48 \times 10^{-2}$	0.875	0.73
23	1.0+0.8	LC	No	No	-7.94	7.28	$3.72 \times 10^{-1}$	$2.18 \times 10^{-2}$	0.889	0.73
24	1.2+0.8	LC	Yes	No	-9.61	7.86	$3.70 \times 10^{-1}$	$1.96 \times 10^{-2}$	0.900	0.71
$v_{\text{ini}} = 200$ km/s		$\Delta y = 0.4 R_{\odot}$								
25	0.8+0.6	O	No	No	-3.65	7.47	$4.61 \times 10^{-1}$	$5.23 \times 10^{-2}$	0.796	0.36
26	0.8+0.8	O	No	No	-4.94	8.74	$4.60 \times 10^{-1}$	$4.54 \times 10^{-2}$	0.820	0.40
27	1.0+0.8	O	No	No	-6.26	9.70	$4.58 \times 10^{-1}$	$3.99 \times 10^{-2}$	0.840	0.40
28	1.2+0.8	O	No	No	-7.60	10.50	$4.57 \times 10^{-1}$	$3.56 \times 10^{-2}$	0.855	0.39
$v_{\text{ini}} = 300$ km/s		$\Delta y = 0.3 R_{\odot}$								
29	0.8+0.6	O	No	No	-3.97	8.39	$4.02 \times 10^{-1}$	$6.96 \times 10^{-2}$	0.705	0.27
30	0.8+0.8	O	No	No	-5.47	9.32	$3.96 \times 10^{-1}$	$6.02 \times 10^{-2}$	0.736	0.30
31	1.0+0.8	O	No	No	-7.04	10.90	$3.90 \times 10^{-1}$	$5.27 \times 10^{-2}$	0.762	0.30
32	1.2+0.8	O	No	No	-8.64	11.80	$3.86 \times 10^{-1}$	$4.69 \times 10^{-2}$	0.783	0.30
$v_{\text{ini}} = 300$ km/s		$\Delta y = 0.4 R_{\odot}$								
33	0.8+0.6	O	No	No	-2.94	11.20	$5.01 \times 10^{-1}$	$1.35 \times 10^{-1}$	0.576	0.14
34	0.8+0.8	O	No	No	-4.13	13.10	$4.89 \times 10^{-1}$	$1.15 \times 10^{-1}$	0.620	0.16
35	1.0+0.8	O	No	No	-5.37	14.62	$4.82 \times 10^{-1}$	$9.97 \times 10^{-2}$	0.657	0.16
36	1.2+0.8	O	No	No	-6.63	15.71	$4.76 \times 10^{-1}$	$8.81 \times 10^{-2}$	0.688	0.16

**Table 2.** Kinematical properties of the simulations reported here involving a  $0.4 M_{\odot}$  white dwarf.

Run	$M_1 + M_2$ ( $M_{\odot}$ )	Outcome	Detonation	Ejection	$E$ ( $10^{48}$ erg)	$L$ ( $10^{50}$ erg s $^{-1}$ )	$r_{\max}$ ( $R_{\odot}$ )	$r_{\min}$ ( $R_{\odot}$ )	$\epsilon$	$\beta$
$v_{\text{ini}} = 75$ km/s		$\Delta y = 0.3 R_{\odot}$								
37	0.2+0.4	DC	Yes	1	-0.84	0.82	$3.65 \times 10^{-1}$	$8.94 \times 10^{-3}$	0.952	3.97
38	0.4+0.4	DC	Yes	2	-1.69	1.23	$3.64 \times 10^{-1}$	$6.65 \times 10^{-3}$	0.964	4.21
$v_{\text{ini}} = 75$ km/s		$\Delta y = 0.4 R_{\odot}$								
39	0.2+0.4	LC	Yes	No	-0.67	1.09	$4.51 \times 10^{-1}$	$1.60 \times 10^{-2}$	0.931	2.21
40	0.4+0.4	DC	Yes	2	-1.35	1.64	$4.50 \times 10^{-1}$	$1.19 \times 10^{-2}$	0.948	2.35
41	0.8+0.4	DC	Yes	1	-2.73	2.18	$4.49 \times 10^{-1}$	$7.85 \times 10^{-3}$	0.966	2.93
42	1.2+0.4	DC	Yes	1	-4.12	2.45	$4.48 \times 10^{-1}$	$5.84 \times 10^{-3}$	0.974	3.26
$v_{\text{ini}} = 100$ km/s		$\Delta y = 0.3 R_{\odot}$								
43	0.2+0.4	LC	Yes	No	-0.81	1.09	$3.68 \times 10^{-1}$	$1.62 \times 10^{-2}$	0.916	2.19
44	0.4+0.4	DC	Yes	2	-1.65	1.64	$3.66 \times 10^{-1}$	$1.20 \times 10^{-2}$	0.937	2.34
45	0.8+0.4	DC	Yes	1	-3.35	2.18	$3.64 \times 10^{-1}$	$7.88 \times 10^{-3}$	0.958	2.92
46	1.2+0.4	DC	Yes	1	-5.07	2.45	$3.63 \times 10^{-1}$	$5.88 \times 10^{-3}$	0.968	3.23
$v_{\text{ini}} = 100$ km/s		$\Delta y = 0.4 R_{\odot}$								
47	0.2+0.4	LC	No	No	-0.64	1.46	$4.55 \times 10^{-1}$	$2.93 \times 10^{-2}$	0.879	1.21
48	0.4+0.4	LC	Yes	No	-1.31	2.18	$4.53 \times 10^{-1}$	$2.16 \times 10^{-2}$	0.909	1.29
49	0.8+0.4	DC	Yes	1	-2.68	2.91	$4.51 \times 10^{-1}$	$1.42 \times 10^{-2}$	0.939	1.62
50	1.2+0.4	DC	Yes	1	-4.07	3.27	$4.50 \times 10^{-1}$	$1.05 \times 10^{-2}$	0.954	1.80
$v_{\text{ini}} = 150$ km/s		$\Delta y = 0.3 R_{\odot}$								
51	0.2+0.4	LC	No	No	-0.74	1.64	$3.81 \times 10^{-1}$	$3.84 \times 10^{-2}$	0.818	0.92
52	0.4+0.4	LC	Yes	No	-1.55	2.46	$3.75 \times 10^{-1}$	$2.81 \times 10^{-2}$	0.861	1.00
53	0.8+0.4	DC	Yes	1	-3.22	3.27	$3.69 \times 10^{-1}$	$1.83 \times 10^{-2}$	0.906	1.26
54	1.2+0.4	DC	Yes	1	-4.92	3.68	$3.67 \times 10^{-1}$	$1.35 \times 10^{-2}$	0.929	1.41
$v_{\text{ini}} = 150$ km/s		$\Delta y = 0.4 R_{\odot}$								
55	0.2+0.4	O	No	No	-0.58	2.18	$4.70 \times 10^{-1}$	$7.14 \times 10^{-2}$	0.736	0.50
56	0.4+0.4	O	No	No	-1.21	3.28	$4.62 \times 10^{-1}$	$5.16 \times 10^{-2}$	0.799	0.54
57	0.8+0.4	LC	Yes	No	-2.55	4.37	$4.56 \times 10^{-1}$	$3.30 \times 10^{-2}$	0.864	0.70
58	1.2+0.4	LC	Yes	No	-3.91	4.91	$4.54 \times 10^{-1}$	$2.44 \times 10^{-2}$	0.898	0.78
$v_{\text{ini}} = 200$ km/s		$\Delta y = 0.3 R_{\odot}$								
59	0.2+0.4	O	No	No	-0.65	2.18	$4.07 \times 10^{-1}$	$7.31 \times 10^{-2}$	0.695	0.49
60	0.4+0.4	O	No	No	-1.41	3.28	$3.90 \times 10^{-1}$	$5.27 \times 10^{-2}$	0.762	0.53
61	0.8+0.4	LC	Yes	No	-3.03	4.36	$3.78 \times 10^{-1}$	$3.36 \times 10^{-2}$	0.837	0.68
62	1.2+0.4	LC	Yes	No	-4.71	4.91	$3.73 \times 10^{-1}$	$2.47 \times 10^{-2}$	0.876	0.77
$v_{\text{ini}} = 200$ km/s		$\Delta y = 0.4 R_{\odot}$								
63	0.2+0.4	O	No	No	-0.48	2.91	$5.05 \times 10^{-1}$	$1.41 \times 10^{-1}$	0.564	0.25
64	0.4+0.4	O	No	No	-1.07	4.37	$4.82 \times 10^{-1}$	$9.97 \times 10^{-2}$	0.657	0.28
65	0.8+0.4	O	No	No	-2.36	5.82	$4.66 \times 10^{-1}$	$6.23 \times 10^{-2}$	0.764	0.37
66	1.2+0.4	LC	Yes	No	-3.70	6.55	$4.60 \times 10^{-1}$	$4.53 \times 10^{-2}$	0.821	0.42
$v_{\text{ini}} = 300$ km/s		$\Delta y = 0.3 R_{\odot}$								
67	0.4+0.4	O	No	No	-1.01	4.91	$4.87 \times 10^{-1}$	$1.33 \times 10^{-1}$	0.571	0.14
68	0.8+0.4	O	No	No	-2.50	6.55	$4.17 \times 10^{-1}$	$8.35 \times 10^{-2}$	0.666	0.28
69	1.2+0.4	O	No	No	-4.11	7.36	$3.96 \times 10^{-1}$	$6.01 \times 10^{-2}$	0.737	0.32
$v_{\text{ini}} = 300$ km/s		$\Delta y = 0.4 R_{\odot}$								
70	0.8+0.4	O	No	No	-1.82	8.74	$5.22 \times 10^{-1}$	$1.63 \times 10^{-1}$	0.525	0.14
71	1.2+0.4	O	No	No	-3.10	9.82	$4.90 \times 10^{-1}$	$1.14 \times 10^{-1}$	0.621	0.17

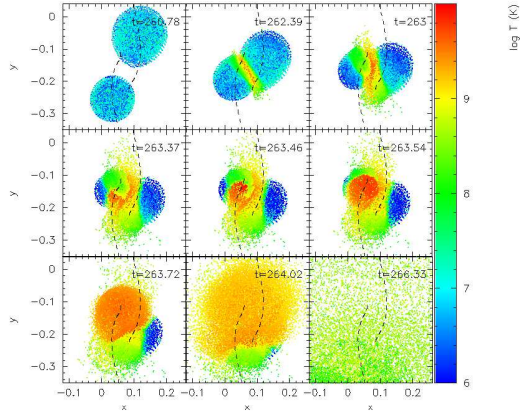


**Figure 1.** Time evolution of one of the simulations in which the dynamical interaction of two white dwarfs results in the disruption of both stars. In particular, this simulation corresponds to the case in which the interacting stars have masses  $0.8 M_{\odot}$  and  $1.0 M_{\odot}$ , whereas the initial velocity is  $v_{\text{ini}} = 100$  km/s and the initial distance is  $\Delta y = 0.3 R_{\odot}$  — that is, run number 7 in Table 1. The temperature of each SPH particle is also shown, expressed in K. The  $x$  and  $y$  axes are in units of  $0.1 R_{\odot}$ . The dashed lines correspond to the trajectories of the center of mass of each intervening star. Only 1 out of 10 particles has been represented. Times (in seconds) since the beginning of the simulation are shown in the right upper corner of each panel. These figures have been done using the visualization tool SPLASH (Price 2007). [Color figure only available in the electronic version of the article].

40% carbon and 60% oxygen (by mass), except for the lightest one — which is made of pure helium — and the heaviest one — which is made of a mixture of 80% of oxygen and 20% of neon, also by mass. The intervening stars were relaxed separately to obtain accurate equilibrium initial configurations, using  $\sim 2 \times 10^5$  particles for each star. This resolution is high enough to provide accurate results and low enough to run a large number of simulations in a reasonable period of time. The initial temperature of our isothermal white dwarf configurations is  $\sim 10^7$  K. As in Lorén-Aguilar et al. (2010), the white dwarfs were assumed to rotate counterclockwise as rigid bodies (Charpinet et al. 2009) with rotational velocities  $\omega \simeq 7 \times 10^{-5}$  rad/s — a typical rotation velocity of field white dwarfs (Berger et al. 2005). This rotation rate is nevertheless irrelevant to the dynamics of the close encounters studied in this paper. In fact, the spin rates of post-capture white dwarfs could be larger, as the capture is dominated by tidal dissipation, which would lead to spin-up of at least the lower mass white dwarf, and of both stars if the masses are comparable (Press & Teukolsky 1977).

We fixed the initial distance between the stars along the  $x$ -axis,  $\Delta x = 0.2 R_{\odot}$ , and allowed the initial distance along the  $y$ -axis to vary between  $\Delta y = 0.3 R_{\odot}$  and  $0.4 R_{\odot}$ . Under these conditions the tidal deformations of both white dwarfs are negligible at the beginning of the simulation and the approximation of spherical symmetry is valid. The initial velocity of each star was set to  $\mathbf{v}_{\text{ini}} = (\pm v_{\text{ini}}, 0, 0)$ , with  $v_{\text{ini}}$  ranging from 75 to 300 km/s, which are typical values for which the interaction ends up in a collision. With this setting the initial coordinates of the two intervening white dwarfs are  $(\Delta x/2, -\Delta y/2, 0)$  and  $(-\Delta x/2, \Delta y/2, 0)$  and the relative velocity is  $2v_{\text{ini}}$ . Note that these initial conditions

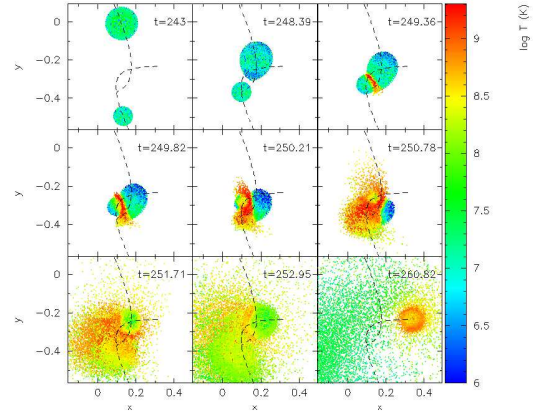


**Figure 2.** Same as Fig. 1 for one of the simulations in which the dynamical interaction results in the disruption of the less massive star, while the more massive white dwarf retains its identity. This specific simulation corresponds to the case in which the initial velocity is  $v_{\text{ini}} = 100$  km/s and the initial distance is  $y_{\text{ini}} = 0.3 R_{\odot}$ , while the masses of the colliding white dwarfs are 0.8 and  $1.2 M_{\odot}$ , respectively, corresponding to simulation number 8 in Table 1. [Color figure only available in the electronic version of the article].

lead in all cases to negative energies, which result in initial elliptical trajectories, although some of them have high eccentricities — see below. That is, the interactions studied here correspond to a post-capture scenario. For a detailed study of the gravitational capture mechanisms see, for example, Press & Teukolsky (1977) and Lee & Ostriker (1986). Additionally, we note that in order for a pair of stars to become bound after a close encounter, some kind of dissipation mechanism must be involved, like a third body tidal interaction (Shara & Hurley 2002), or the excitation of stellar pulsations by means of tidal interaction (Fabian et al. 1975).

## 4 OUTCOMES OF THE INTERACTIONS

### 4.1 Time evolution

In most simulations the time evolution of the interactions computed here is the same found in our previous paper (Lorén-Aguilar et al. 2010). In particular, after tidal interaction, the intervening white dwarfs either form an eccentric binary or collide. In particular, if the intervening stars get sufficiently close at periastron and mass transfer begins, a stellar merger occurs. In this case, two different behaviors can be clearly distinguished. If more than one mass-transfer episode occurs before the stellar merger, we name it a lateral collision (LC). Else, if just one mass transfer happens, then we call the interaction a direct collision (DC). Otherwise, if the binary system survives without transferring mass, an eccentric orbit will be the outcome (O) of the interaction.

Also, for most of the cases studied here in which a collision occurs, the resulting remnants left behind by the dynamical interaction are very similar to those found in our previous work (Lorén-Aguilar et al. 2010). However, there are a few cases in which the interaction is so strong that the material of the lightest white dwarf is ejected from the

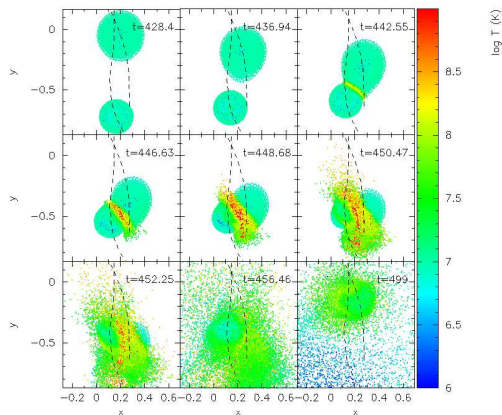


**Figure 3.** Same as Fig. 1 for the simulation in which two helium white dwarfs are involved. In this case the dynamical interaction results in the tidal disruption of an extremely low mass white dwarf of mass  $0.2 M_{\odot}$  in the gravitational field of a  $0.4 M_{\odot}$  helium white dwarf. The initial conditions of this specific simulation are  $v_{\text{ini}} = 75$  km/s and  $y_{\text{ini}} = 0.3 R_{\odot}$ , corresponding to run number 37 in Table 2. [Color figure only available in the electronic version of the article].

system. Finally, there are as well some interactions in which both stars are totally disrupted. This occurs as a consequence of the very high temperatures attained in the contact region during the most violent phase of the dynamical interaction. Specifically, in all the simulations in which one or both stars are disrupted and the material is ejected from the system the temperatures and densities reached during the interaction are high enough to drive a detonation. If the material of the disrupted less massive star is a mixture of carbon and oxygen this occurs when the temperature is larger than  $\sim 2.5 \times 10^9$  K and the density is above  $2.0 \times 10^6$  g cm $^{-3}$  (Seitenzahl et al. 2009; Pakmor et al. 2011). When the less massive white dwarf is made of helium we consider that a detonation is likely to develop when the nuclear timescale is shorter than the dynamical one. Nevertheless, we emphasize that these are only necessary conditions, since whether a detonation develops or not depends as well on other factors, like the temperature and density gradients.

We find that in most of the simulations in which the material of the disrupted low-mass white dwarf reaches high temperatures and large densities the regions in which a detonation is likely to develop comprise a small number of particles and degeneracy is rapidly lifted. Consequently, in these cases the result of the dynamical interaction is not a powerful thermonuclear explosion, leading to a supernova. However, there are a few runs in which the number of particles that reach detonation conditions is large enough to ensure that a supernova occurs. This happens, for instance, in the case in which two heavy carbon-oxygen white dwarfs of masses  $0.8 M_{\odot}$  and  $1.0 M_{\odot}$  interact. The time evolution of this system is depicted in Fig. 1. There are other cases in which only the material of the less massive white dwarf is ejected after being tidally disrupted by the more massive one. This occurs, for instance, when the primary is a very compact oxygen-neon white dwarf. Due to the very small radius of the more massive white dwarf a sizable fraction of the less massive white dwarf is not accreted as it occurs

when two white dwarfs with smaller mass contrast interact but, instead, in this case the oxygen-neon white dwarf is barely affected by the interaction, while the material of the disrupted less massive star bounces on the surface of the primary and is ejected at somewhat large velocities, of the order of  $10^4$  km/s. Fig. 2 shows an example of the temporal evolution in these cases. Specifically, this figure displays the time evolution in the case in which a  $0.8 M_{\odot}$  carbon-oxygen white dwarf and a  $1.2 M_{\odot}$  oxygen-neon white dwarf interact. Finally, there are other simulations in which both stars are disrupted as well although there is not a large mass contrast. This occurs mainly for the simulations involving two helium white dwarfs. Fig. 3 illustrates the case in which an extremely low mass white dwarf of mass  $0.2 M_{\odot}$  white dwarf is tidally disrupted by another helium white dwarf of mass  $0.4 M_{\odot}$ , and its material is ejected from the system. Finally, it is interesting to note as well that in all these simulations the shocked region is well resolved by our simulations — see Figs. 1, 2, and 3.

## 4.2 Overview of the simulations

Tables 1 and 2 list all the simulations performed in this work, grouped as a function of the initial positions and velocities. In particular, Table 1 lists the kinematical properties of the simulations in which a  $0.8 M_{\odot}$  carbon-oxygen white dwarf is involved, whereas in Table 2 we display the same information for the simulations in which a light-weight ( $0.4 M_{\odot}$ ) helium white dwarf is considered. Note that these simulations complement those of Lorén-Aguilar et al. (2010), in which the interaction of two white dwarfs of masses  $0.6$  and  $0.8 M_{\odot}$  was studied. Thus, the present set of simulations, when complemented with those of Lorén-Aguilar et al. (2010), encompasses the most plausible range of white dwarf masses.

In both tables we list the masses of the interacting white dwarfs (second column) and the outcome of the dynamical interaction (third column). The fourth column shows if the physical conditions for a detonation are met during the dynamical interaction, and if as a consequence of the interaction the material of the less massive white dwarf is ejected (1), or if both stars are totally disrupted (2) — fifth column. The total energy,  $E$ , and the total angular momentum,  $L$ , of the system are listed in the sixth and seventh columns, respectively. These two quantities have been computed using the corresponding SPH prescriptions. Note as well that all the energies of the systems considered here are negative and, thus, the initial trajectories are in all cases elliptical. Therefore, the apoastron ( $r_{\text{max}}$ ), the periastron ( $r_{\text{min}}$ ) and the eccentricity ( $\epsilon$ ) of the orbits are also specified in this table — columns 7, 8 and 9, respectively. All these quantities have been computed using the solution of the two-body problem, assuming that the two white dwarfs are point masses. However, it is important to realize that tidal interactions subsequently modify the initial orbits, leading to different outcomes. Finally, in the last column of tables 1 and 2 we also list the so-called impact parameter, which is defined as

$$\beta = \frac{R_1 + R_2}{r_{\text{min}}}, \quad (7)$$

This parameter is a good indicator of the strength of the interaction. In this expression  $R_1$  is the radius of the more massive white dwarf and  $R_2$  that of the less massive one.

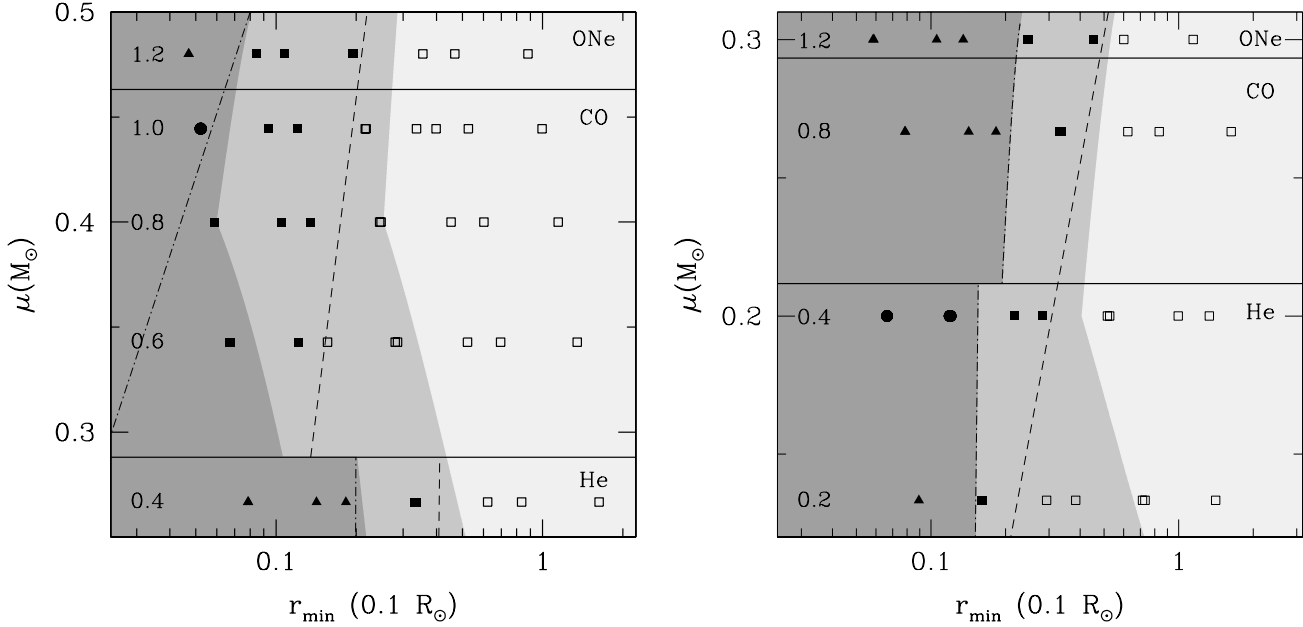


**Figure 4.** Outcomes of the simulations performed here presented in the plane defined by the reduced mass of the system and the periastron distance. The left panel displays the outcomes of the simulations in which a  $0.8 M_{\odot}$  carbon-oxygen white dwarf is involved, whilst the right panel shows the outcomes of the simulations in which a  $0.4 M_{\odot}$  helium white dwarf is used. The shaded areas indicate the regions for which the three different outcomes occur, as explained in the main text. Each row of simulations is also labelled with the mass of the second interacting white dwarf corresponding to the indicated reduced mass. The horizontal solid lines separate the regions of helium, carbon-oxygen and oxygen-neon white dwarfs, respectively. Hollow squares indicate those simulations in which no detonation occurs, filled squares represent those simulations in which the conditions for a detonation are met, filled triangles correspond to those simulations in which the material of the lightest white dwarf is ejected, while filled circles show the simulations in which both white dwarfs are completely destroyed. The dashed line separates the region in which no detonations occur and that in which during the dynamical interaction the physical conditions for a detonation to occur are met, while the dotted-dashed line indicates the region for which the dynamically interacting system is totally or partially disrupted. Those interactions occurring to the left of this line result in an ejection of the material of at least one component of the system.

### 4.3 The outcomes of the interactions

As previously said, our simulations result in three different outcomes, depending on the adopted initial conditions. Not surprisingly, we find that the most relevant physical parameter for discriminating between the three different outcomes is the periastron distance,  $r_{\min}$ . In particular, we find that as the periastron distance decreases, the outcome of the interaction changes from the formation of an eccentric binary to a lateral collision and then to a direct one. This can be seen in Fig. 4, where we show the different outcomes of our simulations as a function of the periastron distance and the reduced mass of the system —  $\mu = M_1 M_2 / (M_1 + M_2)$  — for the case in which the mass of one of the interacting white dwarfs is kept fixed to  $0.8 M_{\odot}$  — left panel — or to  $0.4 M_{\odot}$  — right panel. In these panels the dark grey shaded areas represent the region in which the outcome of the interaction is a direct collision, the medium grey shaded areas show the regions in which lateral collisions occur, while the light grey shaded areas display the regions in which eccentric binaries are formed. We have also labelled, for the sake of clarity, each set of simulations with the mass of the second interacting white dwarf — from  $1.2 M_{\odot}$  to  $0.2 M_{\odot}$ . In this way it is better illustrated how the masses of the white dwarfs involved in the interaction affect the resulting outcome.

To gain insight in the physics of the interaction process we have proceeded as follows. It could be naively expected that a direct collision occurs when at closest approach the

two intervening white dwarfs are in contact. This happens when the minimum distance between their respective centers of mass,  $r_{\min}$ , is smaller than the sum of the unperturbed radii of the white dwarfs. That is, when  $r_{\min} \leq R_1 + R_2$ , where  $R_1$  and  $R_2$  are the radii of both white dwarfs at sufficiently large distances. Instead, our results show that in a direct collision the overlap between both white dwarfs at minimum distance is substantial in all cases, otherwise the less massive star survives the first mass transfer episode and a lateral collision is the outcome of the interaction, and thus this criterion is not valid. There are several reasons for this. The first one is that in direct collisions the relative velocities of the SPH particles are relatively large, or equivalently  $\beta$  is sufficiently large. Thus, in direct collisions the SPH particles of both stars are thoroughly mixed. The second reason is that in this approximation  $r_{\min}$  is computed using the expression for point masses, whereas in our simulations we deal with extended bodies. Thus, in our calculations the distance at closest approach is larger than that obtained using point masses. Finally, tidal forces also decrease the periastron of the system. The interplay between all these factors is complex and, accordingly, the simplistic criterion previously explained has to be modified. To take into account that in all direct collisions substantial overlap at minimum distance occurs we adopt  $r_{\min} \leq \lambda R_1 + R_2$ , where the parameter  $\lambda$  indicates the degree of overlapping between both stars. The division between the regions of direct collisions and lateral collisions in Fig. 4 is best fitted using  $\lambda \approx -0.35$ , meaning



that indeed the overlap has to be relatively large. We note at this point that the value of  $\lambda$  is the same for those simulations in which either carbon-oxygen and oxygen-neon white dwarfs are involved, but not for the case in which helium white dwarfs interact, for which the conditions for a detonation to occur are rather different. Nevertheless, this, in turn, means that this reasoning is relatively robust enough, as it does not depend much on the mass of the white dwarf.

We now go one step forward and we try to explain which is the physical mechanism that makes the difference between those simulations in which a lateral collision occurs and those simulations which end up in the formation of an eccentric binary. It would also be naively expected that a lateral collision occurs when the periastron distance is such that the less massive white dwarf fills its Roche lobe at closest approach, and consequently mass transfer from the lightest intervening white dwarf to the most massive one is enabled. To test this possibility we have used the usual analytical expression of Eggleton (1983):

$$R_L/a = \frac{0.49q^{2/3}}{0.6q^{2/3} + \ln(1 + q^{1/3})} \quad (8)$$

where  $q = M_2/M_1$  is the mass ratio of the interacting stars, and  $a$  is the binary separation, which in our case is  $a = r_{\min}$ . Nevertheless, we emphasize that Eq. (8) is only valid for circular orbits, while we are dealing with highly eccentric orbits. Most importantly, this expression was derived assuming that the interacting stars are spherical, which in our case is not true, as tidal deformations are important at closest approach. Thus, instead of directly using the value of  $R_L$  obtained from the expression above, we multiply it by a factor  $\eta$ , which takes into account all the non-modelled effects. Hence, we expect that the limiting case separating both dynamical regimes is  $R_2 = \eta R_L$ , with  $R_L$  given by Eq. (8).

As can be seen in Fig. 4, the simple argument previously explained works well when  $\eta \sim 0.95$  is adopted, as all the interactions in which an eccentric binary system is formed lay in the lightest shaded area, whilst the region of lateral collisions is also nicely reproduced. It is worth noting as well that this value is the same for the simulations in which a  $0.8 M_\odot$  white dwarf is involved (left panel of Fig. 4) and those in which a  $0.4 M_\odot$  star is adopted (right panel in the same figure). Hence, the value of  $\eta$  is robust, since it does not depend on the composition of the intervening white dwarf (the  $0.4 M_\odot$  white dwarf is made of helium, while the  $0.8 M_\odot$  star is a regular carbon-oxygen white dwarf), or on the specific details of the interaction. Note also that the change in the slope of the boundary between both regions occurs at  $\mu = 0.4 M_\odot$  for the left panel and at  $\mu = 0.2 M_\odot$  for the right panel of Fig. 4. These values correspond to systems in which both intervening white dwarfs have equal masses. In particular, if we consider the left panel of Fig. 4, stars less massive than  $0.8 M_\odot$  have larger radii than the  $0.8 M_\odot$  white dwarf due to the mass-radius relation. Thus, the distances at closest approach for which a Roche-lobe overflow episode occurs are larger, and the reverse is also true. However, for white dwarfs more massive than  $0.8 M_\odot$  the gravitational well is deeper, and consequently lateral collisions occur for larger periastron distances. The interplay between these two effects determines the turn-off in this plane.

In Fig. 4 we also show the regions in the plane defined

by the reduced mass and periastron distance for which the physical conditions for a detonation are met during the interaction. As shown in Figs. 1 and 2 these conditions always occur in the shocked region resulting from the very rapid accretion phase of the disrupted less massive star onto the almost rigid surface of the more massive white dwarf. The regions in which a detonation forms in the contact region between the surface of the more massive star and the material accreted from the disrupted less massive star are located to the left of the dashed line. The dotted-dashed line indicates the edge of the region for which either the less massive star or both are totally disrupted. We note, however, that if the more massive white dwarf is an oxygen-neon white dwarf the material of the less massive white dwarf is not accreted onto this star, but it bounces back. On the contrary if both stars are massive carbon-oxygen white dwarfs, the system is totally disrupted and the result of the interaction is indeed a super-Chandrasekhar Type Ia supernova.

## 5 PHYSICAL PROPERTIES OF THE INTERACTIONS

Quite generally speaking, and except for the few cases discussed previously in which the material of the less massive star is ejected, or in those cases in which both white dwarfs are entirely disrupted, in all those simulations in which a merger occurs, the less massive white dwarf is accreted by the massive companion, and the resulting configuration consists of a central compact object surrounded by a hot corona, and a region where the debris of the interaction can be found. The properties of the debris region depend very much on the masses of the interacting white dwarfs. In particular, if a direct collision occurs, the final configuration is almost spherically symmetric, whereas in lateral collisions a thick, heavy, rotationally-supported disk is formed in all cases, but in those in which the two interacting white dwarfs have equal masses. All these findings are in agreement with those previously obtained by Lorén-Aguilar et al. (2010). We found that in these simulations little mass is ejected from the system, except in some direct collisions, namely those with rather large values of the impact parameter  $\beta$  — see Tables 1 and 3. The hot corona corresponds to material that has been compressed and heated during the collision, and therefore is substantially enriched in heavy elements. The resulting nucleosynthetic pattern follows closely that found in Lorén-Aguilar et al. (2010).

Table 3 shows some important physical quantities of the simulations in which a merger occurs but the material of the less massive white dwarf is not ejected from the remnant. That is, those simulations in which the remnant of the interaction is a single bound object, with the configuration previously described. In particular, in this table we specify the masses of the central remnant ( $M_{\text{WD}}$ ), of the corona ( $M_{\text{corona}}$ ), and of the debris region ( $M_{\text{debris}}$ ). Also listed are the ejected mass ( $M_{\text{ej}}$ ), as well as the radii of the corona and of the debris region —  $R_{\text{corona}}$  and  $R_{\text{debris}}$ . We considered that the newly formed white dwarf is made of all the material which rotates as a rigid solid plus the hot corona, which rotates faster. This includes both the unperturbed more massive star and the accreted material resulting from the disrupted less massive white dwarf. Finally, we also list

**Table 3.** Hydrodynamical results for the simulations in which a collision occurs and the resulting system remains bound.

Run	Detonation ( $M_{\odot}$ )	$M_{\text{WD}}$	$M_{\text{corona}}$ ( $M_{\odot}$ )	$M_{\text{debris}}$ ( $M_{\odot}$ )	$M_{\text{ej}}$ ( $M_{\odot}$ )	$T_{\text{max}}$ (K)	$T_{\text{peak}}$ (K)	$R_{\text{corona}}$ ( $R_{\odot}$ )	$R_{\text{debris}}$ ( $R_{\odot}$ )	$E_{\text{nuc}}$ (erg)
1	Yes	0.90	0.79	0.46	$3.74 \times 10^{-2}$	$5.35 \times 10^8$	$4.37 \times 10^9$	$9.64 \times 10^{-3}$	0.43	$1.09 \times 10^{49}$
2	Yes	1.12	—	0.34	$1.41 \times 10^{-1}$	$4.69 \times 10^8$	$5.44 \times 10^9$	—	0.28	$4.57 \times 10^{49}$
5	Yes	0.87	0.79	0.50	$3.22 \times 10^{-2}$	$4.90 \times 10^8$	$4.50 \times 10^9$	$8.86 \times 10^{-3}$	0.22	$9.81 \times 10^{48}$
6	Yes	1.13	—	0.33	$1.37 \times 10^{-1}$	$4.65 \times 10^8$	$5.37 \times 10^9$	—	0.19	$4.25 \times 10^{49}$
9	Yes	0.91	0.72	0.48	$1.39 \times 10^{-2}$	$4.79 \times 10^8$	$3.03 \times 10^9$	$8.00 \times 10^{-3}$	0.21	$9.93 \times 10^{47}$
10	Yes	1.29	—	0.28	$2.63 \times 10^{-2}$	$4.50 \times 10^8$	$4.20 \times 10^9$	—	0.21	$2.27 \times 10^{48}$
11	Yes	1.12	0.89	0.64	$4.64 \times 10^{-2}$	$7.77 \times 10^8$	$4.51 \times 10^9$	$6.93 \times 10^{-3}$	0.24	$1.66 \times 10^{49}$
12	Yes	1.26	0.54	0.64	$1.01 \times 10^{-1}$	$1.08 \times 10^9$	$4.66 \times 10^9$	$4.98 \times 10^{-3}$	0.21	$3.67 \times 10^{49}$
13	No	0.91	0.71	0.48	$7.96 \times 10^{-3}$	$4.49 \times 10^8$	$2.18 \times 10^9$	$8.05 \times 10^{-3}$	0.22	$1.49 \times 10^{46}$
14	Yes	1.30	—	0.29	$8.44 \times 10^{-3}$	$4.44 \times 10^8$	$3.50 \times 10^9$	—	0.23	$5.24 \times 10^{47}$
15	Yes	1.15	0.83	0.63	$1.85 \times 10^{-2}$	$7.54 \times 10^8$	$3.89 \times 10^9$	$6.62 \times 10^{-3}$	0.20	$2.63 \times 10^{48}$
16	Yes	1.26	0.54	0.67	$6.81 \times 10^{-2}$	$1.07 \times 10^9$	$4.30 \times 10^9$	$5.02 \times 10^{-3}$	0.19	$2.36 \times 10^{49}$
17	No	0.91	0.41	0.47	$1.41 \times 10^{-2}$	$4.36 \times 10^8$	$1.16 \times 10^9$	$5.44 \times 10^{-3}$	0.38	$1.88 \times 10^{41}$
18	No	1.38	—	0.21	$5.76 \times 10^{-3}$	$3.49 \times 10^8$	$2.54 \times 10^9$	—	0.25	$7.95 \times 10^{46}$
19	No	1.16	0.63	0.62	$1.71 \times 10^{-2}$	$7.02 \times 10^8$	$2.08 \times 10^9$	$4.85 \times 10^{-3}$	0.37	$8.17 \times 10^{45}$
20	Yes	1.31	0.44	0.66	$2.70 \times 10^{-2}$	$1.25 \times 10^9$	$2.80 \times 10^9$	$3.65 \times 10^{-3}$	0.36	$1.43 \times 10^{48}$
21	No	0.92	0.42	0.46	$1.39 \times 10^{-2}$	$4.21 \times 10^8$	$9.22 \times 10^8$	$5.43 \times 10^{-3}$	0.49	$1.90 \times 10^{39}$
22	No	1.33	—	0.27	$4.80 \times 10^{-3}$	$2.48 \times 10^8$	$1.32 \times 10^9$	—	0.43	$8.67 \times 10^{43}$
23	No	1.17	0.50	0.62	$1.73 \times 10^{-2}$	$7.56 \times 10^8$	$1.79 \times 10^9$	$4.81 \times 10^{-3}$	0.34	$9.95 \times 10^{45}$
24	Yes	1.30	0.44	0.67	$2.62 \times 10^{-2}$	$1.17 \times 10^9$	$2.74 \times 10^9$	$3.72 \times 10^{-3}$	0.28	$9.38 \times 10^{47}$
39	Yes	0.42	0.23	0.16	$2.43 \times 10^{-2}$	$1.21 \times 10^8$	$2.29 \times 10^9$	$1.41 \times 10^{-2}$	0.75	$2.04 \times 10^{48}$
43	Yes	0.41	0.22	0.16	$2.26 \times 10^{-2}$	$1.13 \times 10^8$	$2.42 \times 10^9$	$1.18 \times 10^{-2}$	0.49	$2.17 \times 10^{48}$
47	No	0.45	0.24	0.15	$2.54 \times 10^{-3}$	$1.09 \times 10^8$	$6.83 \times 10^8$	$1.63 \times 10^{-2}$	0.57	$1.24 \times 10^{45}$
48	Yes	0.54	—	0.21	$4.81 \times 10^{-2}$	$8.81 \times 10^7$	$2.68 \times 10^9$	—	0.55	$8.49 \times 10^{48}$
51	No	0.44	0.17	0.16	$5.63 \times 10^{-3}$	$1.12 \times 10^8$	$3.96 \times 10^8$	$1.09 \times 10^{-2}$	0.65	$2.75 \times 10^{43}$
52	Yes	0.67	—	0.13	$4.96 \times 10^{-3}$	$8.48 \times 10^7$	$2.29 \times 10^9$	—	0.64	$8.12 \times 10^{47}$
57	Yes	0.85	0.29	0.32	$3.13 \times 10^{-2}$	$4.25 \times 10^8$	$2.50 \times 10^9$	$9.27 \times 10^{-3}$	0.38	$6.09 \times 10^{48}$
58	Yes	1.20	0.27	0.32	$7.80 \times 10^{-2}$	$7.74 \times 10^8$	$2.75 \times 10^9$	$5.34 \times 10^{-3}$	0.41	$2.03 \times 10^{49}$
61	Yes	0.85	0.28	0.32	$2.52 \times 10^{-2}$	$4.13 \times 10^8$	$1.98 \times 10^9$	$9.50 \times 10^{-3}$	0.33	$4.70 \times 10^{48}$
62	Yes	1.21	0.15	0.30	$9.15 \times 10^{-2}$	$7.96 \times 10^8$	$2.74 \times 10^9$	$5.77 \times 10^{-3}$	0.45	$2.53 \times 10^{49}$
66	Yes	1.20	0.15	0.35	$5.15 \times 10^{-2}$	$7.77 \times 10^8$	$2.46 \times 10^9$	$3.35 \times 10^{-3}$	0.74	$1.86 \times 10^{49}$

the maximum temperature of the central remnant at the end of our simulations —  $T_{\text{max}}$  — the maximum temperature achieved during the most violent phase of the merger —  $T_{\text{peak}}$  — and the energy released by nuclear reactions,  $E_{\text{nuc}}$ .

As can be seen in Table 3, when the masses of the intervening white dwarfs are rather different — namely, when the mass difference between both stars is  $\gtrsim 0.2 M_{\odot}$  — the interaction is more violent. This is the case, for instance, of simulation number 5, in which two carbon-oxygen white dwarfs of masses  $0.8 M_{\odot}$  and  $0.6 M_{\odot}$ , respectively, are involved. This occurs because in these cases the less massive white dwarf is destroyed very rapidly in the deep potential well of the more massive one. Moreover, in these simulations the more massive white dwarf has a small radius, which leads to significant accelerations of the material of the disrupted less massive white dwarf, and consequently to stronger interactions. Furthermore, when the masses of the white dwarfs are very different the resulting white dwarf accretes only a small percentage of the less massive star. If the dynamical interaction results in a lateral collision, a large amount of mass of the disrupted less massive white dwarf is incorporated to the debris region, whilst if the interaction results in a direct collision the mass ejected from the system is larger. All these physical considerations are also valid for the sim-

ulations in which a very massive oxygen-neon white dwarf of mass  $1.2 M_{\odot}$  and a  $0.8 M_{\odot}$  carbon-oxygen white dwarf are involved but a lateral collision occurs — namely, simulations 12, 16, 20, and 24. In these simulations we find that a larger fraction of the less massive white dwarf is ejected from the system, while the mass of the debris region is also significantly larger. On the contrary, when the mass difference between the interacting white dwarfs is smaller our calculations show the interaction is more gentle and a sizable amount of mass is accreted on the undisrupted more massive white dwarf. Finally, it is important to realize as well that in all simulations with small impact parameters, which produce lateral collisions, the number of mass transfer episodes is larger for decreasing values in the difference of masses of the interacting white dwarfs.

There is one simulation in which the remnant white dwarf is very close to the Chandrasekhar mass, namely simulation 18. In this simulation two  $0.8 M_{\odot}$  white dwarfs interact. Nevertheless, the remnant is rotating rapidly (a consequence of the conversion of orbital angular momentum in rotational velocity of the remnant), and thus the central density is not extraordinarily large. This prevents the onset of electron captures on  $^{16}\text{O}$  in the densest regions of the remnant. Additionally, in some simulations the temperatures and densities attained during the interaction are high

**Table 4.** Hydrodynamical results for the simulations in which at least the material of one of the colliding stars does not remain bound to the remnant.

Run	Remnant	$M_{\text{WD}}$ ( $M_{\odot}$ )	$M_{\text{debris}}$ ( $M_{\odot}$ )	$M_{\text{ej}}$ ( $M_{\odot}$ )	$v_{\text{ej}}$ (km/s)	$T_{\text{max}}$ (K)	$T_{\text{peak}}$ (K)	$E_{\text{nuc}}$ (erg)
3	No	—	—	1.80	—	—	$1.70 \times 10^{10}$	$1.42 \times 10^{51}$
4	Yes	1.20	0.37	0.43	$6.06 \times 10^3$	$7.89 \times 10^8$	$9.00 \times 10^9$	$1.35 \times 10^{50}$
7	No	—	—	1.80	—	—	$1.70 \times 10^{10}$	$1.72 \times 10^{51}$
8	Yes	1.20	0.39	0.41	$5.95 \times 10^3$	$7.66 \times 10^8$	$8.51 \times 10^9$	$1.42 \times 10^{50}$
37	Yes	0.37	0.06	0.16	$3.19 \times 10^3$	$9.16 \times 10^7$	$2.75 \times 10^9$	$1.61 \times 10^{49}$
38	No	—	—	0.80	—	—	$4.02 \times 10^9$	$7.45 \times 10^{50}$
40	No	—	—	0.80	—	—	$4.03 \times 10^9$	$7.24 \times 10^{50}$
41	Yes	0.78	0.02	0.41	$1.22 \times 10^4$	$2.76 \times 10^8$	$3.57 \times 10^9$	$3.67 \times 10^{50}$
42	Yes	1.20	0.01	0.39	$1.30 \times 10^4$	$7.08 \times 10^8$	$3.97 \times 10^9$	$3.76 \times 10^{50}$
44	No	—	—	0.80	—	—	$4.06 \times 10^9$	$7.38 \times 10^{50}$
45	Yes	0.77	0.02	0.41	$1.22 \times 10^4$	$3.05 \times 10^8$	$3.66 \times 10^9$	$3.66 \times 10^{50}$
46	Yes	1.20	0.01	0.39	$1.32 \times 10^4$	$7.14 \times 10^8$	$4.18 \times 10^9$	$3.93 \times 10^{50}$
49	Yes	0.79	0.01	0.40	$1.21 \times 10^4$	$2.63 \times 10^8$	$3.57 \times 10^9$	$3.46 \times 10^{50}$
50	Yes	1.20	0.01	0.39	$1.29 \times 10^4$	$6.89 \times 10^8$	$3.58 \times 10^9$	$3.67 \times 10^{50}$
53	Yes	0.80	0.01	0.40	$1.15 \times 10^4$	$2.03 \times 10^8$	$3.54 \times 10^9$	$3.16 \times 10^{50}$
54	Yes	1.20	0.01	0.40	$1.27 \times 10^4$	$6.99 \times 10^8$	$3.62 \times 10^9$	$3.58 \times 10^{50}$

enough to drive a detonation. However, in these simulations the regions in which a detonation is likely to develop comprise a small number of particles and degeneracy is rapidly lifted. Consequently, in these cases the result of the dynamical interaction is not a powerful thermonuclear explosion, leading to a supernova.

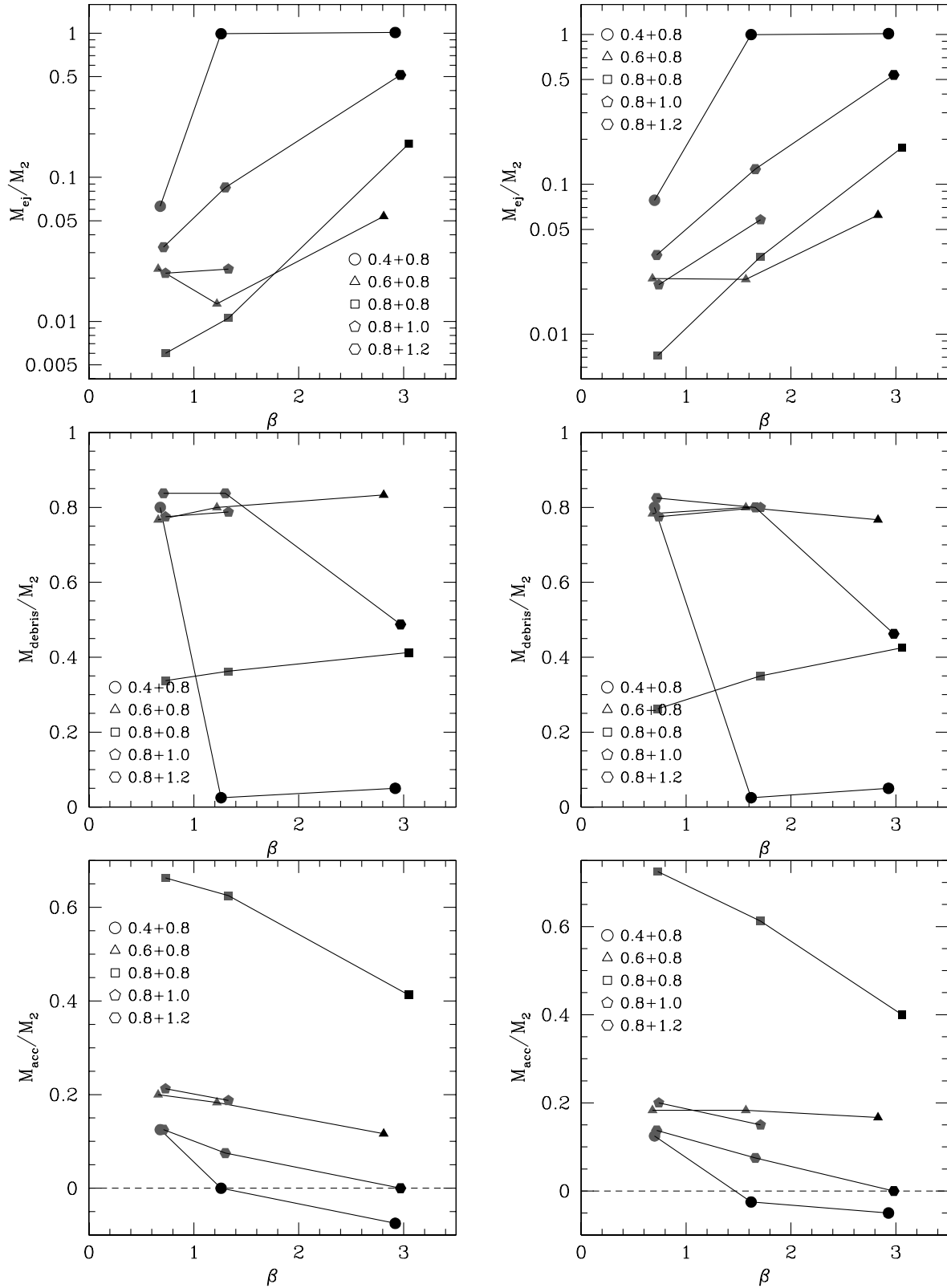
There are a few simulations in which a corona is not formed. These are simulations 2, 6, 10, 14, 18, 22, 48 and 52. All these simulations correspond to interactions in which two equal-mass white dwarfs are involved (with either carbon-oxygen or helium internal chemical compositions). In these cases both white dwarfs are disrupted and merge forming a new, more massive, white dwarf. In particular, the final remnant is always  $\sim 35\%$  more massive than the original white dwarf. Moreover, in these simulations mixing of the disrupted white dwarfs is extensive, and the final temperature profile of the remnant is completely different from that obtained in the rest of the simulations. In fact, the final remnant is isothermal and very hot. Since the nuclear energy release in these simulations is modest, these very high temperatures are the result of compression of the disrupted stars.

Table 4 displays the results obtained in those simulations in which either the material of the less massive star is not accreted by the more massive white dwarf, and thus goes to the debris region or is ejected, or those calculations in which both stars are totally disrupted. Specifically, for each run we first list if a remnant white dwarf exists, the corresponding mass of the remnant white dwarf, the mass of the debris region, the ejected mass, the velocity of the ejecta, the maximum and peak temperatures — as previously defined — attained during the dynamical interaction, and the nuclear energy released.

As can be seen, in most of these simulations a  $0.4 M_{\odot}$  helium white dwarf is involved, although there are a few runs in which the intervening star is an otherwise regular, not extremely massive,  $0.8 M_{\odot}$  carbon-oxygen white dwarf. This

is the case of simulations 3, 4, 7 and 8. This can be easily understood as the combination of two factors. On one hand, the material of the disrupted less massive helium white dwarf has a reduced Coulomb barrier and, hence, nuclear reactions are more easily driven by the dynamical interaction. On the other, a light-weight helium white dwarf has a reduced gravity and, consequently, a larger radius. Thus, it is disrupted at larger distances from the more massive white dwarf, and consequently the material flowing to the primary can be significantly compressed and heated during the interaction. All this results in an explosive behavior. However, in none of these simulations the total mass of the system is larger than Chandrasekhar’s mass, and thus although a powerful nuclear outburst is powered by the conversion of gravitational energy in thermal energy, and a significant amount of nuclear energy is released (of the order of a few times  $10^{50}$  erg) in most cases this energy is invested in ejecting the shocked material (approximately  $0.4 M_{\odot}$ ) at significant velocities (typically  $10^4$  km/s). Of these calculations there are two (namely, runs 3 and 7) in which the outcome is likely a super-Chandrasekhar Type Ia supernova, since in this case both stars are regular carbon-oxygen white dwarfs, although rather massive ( $1.0 M_{\odot}$  and  $0.8 M_{\odot}$ , respectively), the peak temperatures are very large — in excess of  $10^{10}$  K, and no remnant is left after the interaction. In these two simulations the released nuclear energies are very high ( $\sim 1.4 \times 10^{51}$  erg and  $\sim 1.7 \times 10^{50}$  erg, respectively), but these values should be considered as rough estimates, as nuclear statistical equilibrium is not implemented in our code. In runs 4 and 8 a heavy-weight oxygen-neon white dwarf tidally disrupts a carbon-oxygen white dwarf, but the more massive star remains bound, and approximately half of the material of the disrupted star remains orbiting in the debris region, whereas the rest of the material is ejected at considerably large velocities ( $\sim 6 \times 10^3$  km/s). In these two cases the nuclear energy released is somewhat smaller, of the order of  $1.4 \times 10^{50}$  erg.

All this is illustrated in a different way in Fig. 5, where



**Figure 5.** Fraction of mass of the less massive white dwarf ejected (top panels), fraction of the disrupted star that forms the debris region (middle panels) and fraction of mass which is accreted onto the more massive white dwarf (bottom panels) as a function of the impact parameter  $\beta$ , for the simulations in which a  $0.8 M_{\odot}$  white dwarf is involved and a merger occurs. The left panels correspond to the simulations in which  $\Delta y = 0.3 R_{\odot}$  was adopted, whereas in the right panels the simulations in which  $\Delta y = 0.4 R_{\odot}$  was used are displayed. The masses of the intervening white dwarfs and the meaning of the symbols can be found in the respective insets. The grey symbols indicate a lateral collision, while the black ones indicate a direct collision. See text for additional details.

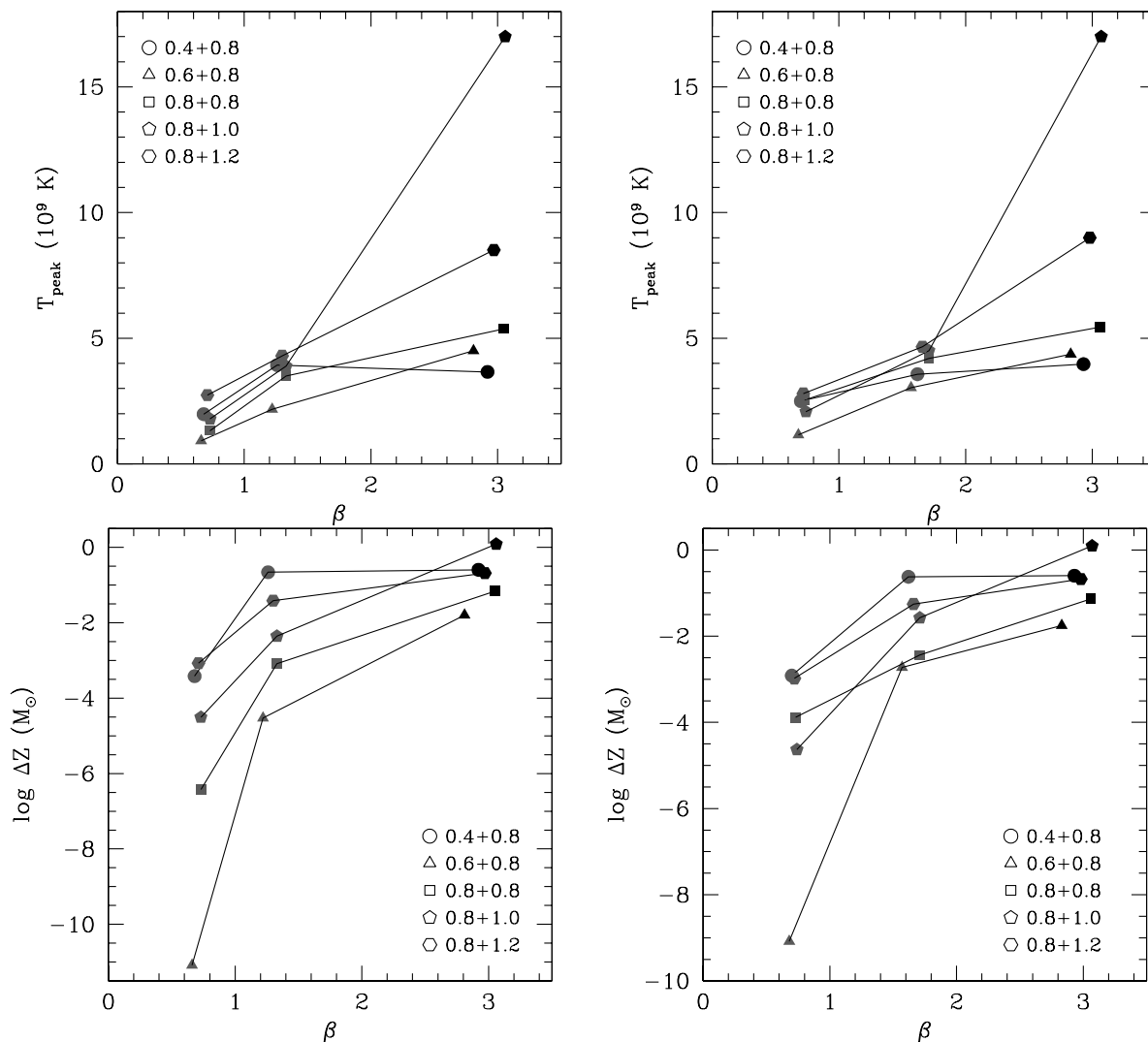


**Figure 6.** Peak temperature achieved during the interaction (top panels) and metallicity enhancement (bottom panels) as a function of the impact parameter  $\beta$ , for the simulations in which a  $0.8 M_{\odot}$  white dwarf is involved and a merger occurs. The left panels correspond to the simulations in which  $\Delta y = 0.3 R_{\odot}$  was adopted, whereas in the right panels the simulations in which  $\Delta y = 0.4 R_{\odot}$  was used are displayed. The masses of the merging white dwarfs and the meaning of the symbols can be found in the respective insets. As in Fig. 5 the black symbols indicate a direct collision, while the grey ones are used to display lateral ones.

we show, for the case in which a  $0.8 M_{\odot}$  carbon-oxygen white dwarf is involved, the fraction of mass of the less massive white dwarf ejected during the interaction — top panels — the fraction of the disrupted star that forms the debris region — middle panels — and the mass fraction accreted by the undisrupted massive white dwarf — bottom panels — as a function of the impact parameter,  $\beta$ . The black, solid symbols are used to depict a direct collision, while the grey ones indicate a lateral one. Note that direct collisions always occur for large values of  $\beta$ . The left panels show the results obtained when  $\Delta y = 0.3 R_{\odot}$ , while the right panels display the results when  $\Delta y = 0.4 R_{\odot}$ .

We start discussing the top panels of Fig. 5. As can be seen in these panels, the fraction of mass ejected during the interaction is small when a lateral collision occurs, of the order of 10% at most. Moreover, for a given set of masses, the mass ejected during the interaction increases for increasing values of  $\beta$ . The only exception is the case in which two white dwarfs of masses  $0.8 M_{\odot}$  and  $0.6 M_{\odot}$  interact. For

these runs the ejected mass first decreases slightly as  $\beta$  increases, and then increases, as in the rest of the simulations. It is important to realize that the mass ejected from the system depends noticeably not only on the masses of the interacting white dwarfs, but also on the peak temperatures achieved during the first and most violent moments of the interaction — which are larger when both stars are rather massive and have similar masses — as well as on other details of each simulation, like the chemical composition of the interacting white dwarfs. This explains why we obtain in this case a different behavior. Note as well that the mass ejected in direct collisions is considerably larger, and in some extreme cases — for instance, in the case in which a  $0.8 M_{\odot}$  and a  $0.4 M_{\odot}$  white dwarf interact — all the mass of the less massive star is ejected from the system. Additionally, comparing the top left and right panels it turns out that all this is nearly independent of the adopted initial distance along the  $y$ -axis,  $\Delta y$ . This can be easily understood. If  $\beta$  is fixed, then all that  $\Delta y$  controls is the eccentricity of the

**Table 5.** Mass abundances of selected chemical elements (Mg, Si, and Fe), for the simulations in which a  $0.8 M_{\odot}$  and a  $0.6 M_{\odot}$  white dwarfs collide and form a bound remnant.

Run	1	5	9	13	17	21
$\beta$	2.83	2.81	1.57	1.22	0.68	0.66
$T_{\text{peak}}$	$4.37 \times 10^9$	$4.50 \times 10^9$	$3.03 \times 10^9$	$2.18 \times 10^9$	$1.16 \times 10^9$	$9.22 \times 10^8$
Maximum abundances						
Mg	$2.36 \times 10^{-1}$	$2.33 \times 10^{-1}$	$2.33 \times 10^{-1}$	$2.12 \times 10^{-1}$	$8.00 \times 10^{-11}$	$1.95 \times 10^{-14}$
Si	$5.86 \times 10^{-1}$	$5.76 \times 10^{-1}$	$2.39 \times 10^{-1}$	$1.43 \times 10^{-1}$	$1.31 \times 10^{-16}$	$1.51 \times 10^{-21}$
Fe	$3.54 \times 10^{-3}$	$1.06 \times 10^{-3}$	$5.03 \times 10^{-24}$	$6.35 \times 10^{-27}$	$5.20 \times 10^{-34}$	$5.20 \times 10^{-34}$
Hot corona						
$\langle \text{Mg} \rangle$	$1.98 \times 10^{-7}$	$4.14 \times 10^{-7}$	$9.87 \times 10^{-8}$	$1.53 \times 10^{-12}$	$1.50 \times 10^{-22}$	$3.12 \times 10^{-24}$
$\langle \text{Si} \rangle$	$1.50 \times 10^{-9}$	$6.04 \times 10^{-9}$	$5.51 \times 10^{-10}$	$6.64 \times 10^{-17}$	$3.38 \times 10^{-31}$	$1.03 \times 10^{-33}$
$\langle \text{Fe} \rangle$	$5.20 \times 10^{-34}$	$5.20 \times 10^{-34}$	$5.19 \times 10^{-34}$	$5.20 \times 10^{-34}$	$5.15 \times 10^{-34}$	$5.09 \times 10^{-34}$
Debris region						
$\langle \text{Mg} \rangle$	$2.97 \times 10^{-3}$	$2.74 \times 10^{-3}$	$1.16 \times 10^{-3}$	$2.48 \times 10^{-5}$	$1.04 \times 10^{-14}$	$2.28 \times 10^{-18}$
$\langle \text{Si} \rangle$	$7.17 \times 10^{-3}$	$5.71 \times 10^{-3}$	$5.84 \times 10^{-4}$	$1.16 \times 10^{-5}$	$1.57 \times 10^{-20}$	$1.30 \times 10^{-25}$
$\langle \text{Fe} \rangle$	$5.14 \times 10^{-7}$	$2.60 \times 10^{-7}$	$4.49 \times 10^{-28}$	$3.81 \times 10^{-31}$	$4.63 \times 10^{-34}$	$4.42 \times 10^{-34}$
Ejecta						
$\langle \text{Mg} \rangle$	$5.92 \times 10^{-2}$	$5.81 \times 10^{-2}$	$1.58 \times 10^{-2}$	$5.72 \times 10^{-10}$	$6.38 \times 10^{-18}$	$3.24 \times 10^{-17}$
$\langle \text{Si} \rangle$	$1.27 \times 10^{-1}$	$1.29 \times 10^{-1}$	$9.27 \times 10^{-3}$	$3.84 \times 10^{-14}$	$3.07 \times 10^{-25}$	$2.73 \times 10^{-24}$
$\langle \text{Fe} \rangle$	$2.16 \times 10^{-6}$	$3.15 \times 10^{-6}$	$2.97 \times 10^{-27}$	$4.10 \times 10^{-34}$	$5.20 \times 10^{-34}$	$5.20 \times 10^{-34}$

encounter, and the eccentricity varies very little for the  $\Delta y$  values chosen.

Now we turn our attention to the mass of the debris region — middle panels of Fig. 5. As can be seen, when the mass contrast is large (say  $\gtrsim 0.3 M_{\odot}$ ) the mass of the debris region decreases for increasing values of  $\beta$ , whereas in all other cases the fraction of the less massive white dwarf which goes to form the debris region slightly increases as for larger values of  $\beta$ . Note as well that, as it occurs with the mass ejected from the system, the general trend is nearly independent of the adopted value of  $\Delta y$ . Finally, we discuss the mass accreted by the more massive white dwarf — bottom panels of Fig. 5. As previously mentioned, the final mass of the remnant white dwarf is the mass of the undisturbed massive component of the system and the mass of the hot corona that is formed during the interaction. Our simulations demonstrate that for strong impacts — or, equivalently, large values of  $\beta$  — the accreted mass decreases substantially as  $\beta$  increases. Actually, the accreted mass can be negative for relatively large values of  $\beta$ . This means that actually some material of the more massive white dwarf is removed during interaction and is ejected or incorporated into the debris region. This occurs for the case in which a  $0.4 M_{\odot}$  helium white dwarf interacts with a  $0.8 M_{\odot}$  carbon-oxygen one. In the rest of the cases — except in that in which two equal-mass  $0.8 M_{\odot}$  interact — the accreted mass is  $\sim 20\%$  in lateral collisions and much smaller in direct ones. As mentioned, the exception to this general rule is the previously mentioned case in which two  $0.8 M_{\odot}$  white dwarfs collide. In this case the fraction of mass incorporated to the remnant is considerably larger, typically  $\sim 50\%$ . Finally, we emphasize that, again, all these considerations are independent of  $\Delta y$ , for the same reason previously discussed.

Finally, to close this section we discuss Fig. 6, where we show the peak temperatures reached during the interactions in which a  $0.8 M_{\odot}$  white dwarf is involved, as a function of the impact parameter  $\beta$  — top panels — and the corresponding metallicity enhancements due to nuclear reactions — bottom panels. As in Fig. 5 the left panels show the cases in which  $\Delta y = 0.3 R_{\odot}$  was adopted, whereas the right panels show the cases in which  $\Delta y = 0.4 R_{\odot}$  was used. We also use the same convention adopted in Fig. 5, and the grey symbols indicate a lateral collision, while the black ones denote a direct one. As in Fig. 5 the masses of the colliding white dwarf are indicated in the insets of each figure. As can be seen in this figure, the peak temperatures reached during the interaction — top panels — increase for increasing values of  $\beta$  in almost all cases. It is worth noticing that, except for the case in which a  $0.8 M_{\odot}$  and a  $1.0 M_{\odot}$  white dwarfs interact, the relationship between  $T_{\text{peak}}$  and  $\beta$  is almost linear. Note that in the case in which two rather massive carbon-oxygen white dwarfs of masses  $1.0 M_{\odot}$  and  $0.8 M_{\odot}$  directly collide the resulting peak temperature is rather large,  $T_{\text{peak}} \simeq 1.7 \times 10^{10}$ . As previously found for the masses ejected from the system, accreted to the central remnant, and incorporated to the debris region, the behavior of the peak temperature as a function of  $\beta$  is almost independent of the adopted value of  $\Delta y$ . Another important characteristic is that, in general, the larger the total mass of the system, the higher the peak temperature reached during the interaction. Additionally, we find that the more violent the interaction — and, consequently, the larger the mass transfer rate — the higher the peak temperatures are. This is a natural consequence of the matter of the disrupted less massive star being more rapidly compressed in these interactions. We now turn our attention to the bottom panels

of this figure, we show the metallicity enhancement,  $\Delta Z$ , resulting from our simulations. Here we define  $\Delta Z$  as the sum of the mass abundances of all elements that were not present in the original white dwarfs plus helium. For example, if the two intervening white dwarfs are made of carbon-oxygen  $\Delta Z$  stands for the sum of the abundances of all elements heavier than oxygen. As can be seen in these panels, the metallicity enhancement increases abruptly until a critical value of  $\beta$ , while for values of  $\beta$  larger than the critical one the metallicity enhancement also increases but with a shallower slope. Examining the left and right panels of Fig. 6 it turns out that this critical value lies between  $\beta \sim 1.2$  and  $\sim 1.6$ . All this is, obviously, the result of the high temperatures reached during the dynamical interactions, and hence the metallicity enhancement shows the same overall behavior observed for the peak temperatures. However, due to the strong dependence of the thermonuclear reaction rates on temperature the slopes of the relationship between  $\Delta Z$  and  $\beta$  are much steeper (note that the bottom panels of Fig. 6 have a logarithmic scale).

It is as well interesting to note that the nucleosynthetic endpoint depends sensitively on  $\beta$ , as it should be expected. This is illustrated in Table 5 where we list the abundances of some selected chemical species for the simulations in which a  $0.8 M_{\odot}$  and a  $0.6 M_{\odot}$  white dwarfs collide and form a bound remnant, which is a representative case of the calculations reported here. Specifically, for these runs we list the respective impact parameter, the peak temperature reached during the interaction and the abundances (by mass) of magnesium, silicon and iron in the hot corona, in the debris region and in the ejecta. We also list the maximum abundances of these elements found in the entire remnant. We note that these abundances are in line with those found by Lorén-Aguilar et al. (2010). The first thing to be noted in this table is that the larger the value of  $\beta$  — and, consequently, of  $T_{\text{peak}}$  — the more extensive nuclear processing is and the larger the maximum abundances of these elements. Secondly, it is important to realize that the average abundances of these elements are largest in the ejecta, while they are rather small in the hot corona and have sizeable values in the debris region. This, in turn, is a consequence of the very intensive nuclear processing of the shocked material hitting the rigid surface of the more massive white dwarf and acquiring very large velocities during the interaction, which results in the subsequent ejection of these particles. This is particularly true for runs 1 and 5. Note that for these simulations the iron and silicon abundances are very large, and that the silicon abundance is larger than that of magnesium and iron, indicating that nuclear processing has been very extensive, but has not been complete. Magnesium is the most abundant isotope in the ejecta of run 9, and its abundance decreases abruptly for successive runs, while silicon is the most abundant element maximum in the ejecta of runs 1 and 5. For these simulations the iron abundance is also maximum, but for  $\beta \lesssim 1.6$  becomes negligible. The same behavior is found for the debris region. Finally, we emphasize that the iron abundance is negligible in the hot corona, independently of the value of  $\beta$ , whilst the magnesium and silicon abundances are modest there.

Finally, table 6 lists the mass of  $^{56}\text{Ni}$  synthesized in those simulations in which a detonation occurs, and the corresponding energy release according to the simple scaling

**Table 6.**  $^{56}\text{Ni}$  production in the collisions that have undergone a detonation.

Run	Ejection	$M_{\text{Ni}}$ ( $M_{\odot}$ )	$L$ erg/s
1	No	$8.65 \times 10^{-8}$	$1.79 \times 10^{36}$
2	No	$4.47 \times 10^{-3}$	$9.23 \times 10^{40}$
3	2	$7.25 \times 10^{-1}$	$1.50 \times 10^{43}$
4	1	$6.60 \times 10^{-2}$	$1.36 \times 10^{42}$
5	No	$2.74 \times 10^{-8}$	$5.66 \times 10^{35}$
6	No	$3.67 \times 10^{-3}$	$7.58 \times 10^{40}$
7	2	$7.15 \times 10^{-1}$	$1.48 \times 10^{43}$
8	1	$6.32 \times 10^{-2}$	$1.31 \times 10^{42}$
9	No	$7.89 \times 10^{-34}$	$1.63 \times 10^{10}$
10	No	$4.52 \times 10^{-10}$	$9.33 \times 10^{33}$
11	No	$7.94 \times 10^{-7}$	$1.64 \times 10^{37}$
12	No	$1.09 \times 10^{-5}$	$2.25 \times 10^{38}$
14	No	$7.44 \times 10^{-16}$	$1.54 \times 10^{28}$
15	No	$1.56 \times 10^{-13}$	$3.22 \times 10^{30}$
16	No	$9.70 \times 10^{-10}$	$2.00 \times 10^{34}$
20	No	$1.12 \times 10^{-33}$	$2.31 \times 10^{10}$
24	No	$1.12 \times 10^{-33}$	$2.31 \times 10^{10}$
37	1	$1.31 \times 10^{-9}$	$2.71 \times 10^{34}$
38	2	$8.84 \times 10^{-4}$	$1.83 \times 10^{40}$
39	No	$5.57 \times 10^{-16}$	$1.15 \times 10^{28}$
40	2	$1.64 \times 10^{-3}$	$3.39 \times 10^{40}$
41	1	$8.04 \times 10^{-4}$	$1.66 \times 10^{40}$
42	1	$1.18 \times 10^{-3}$	$2.44 \times 10^{40}$
43	No	$4.97 \times 10^{-14}$	$1.03 \times 10^{30}$
44	2	$4.68 \times 10^{-3}$	$9.67 \times 10^{40}$
45	1	$7.60 \times 10^{-4}$	$1.57 \times 10^{40}$
46	1	$2.21 \times 10^{-3}$	$4.56 \times 10^{40}$
48	No	$2.76 \times 10^{-11}$	$5.70 \times 10^{32}$
49	1	$5.00 \times 10^{-4}$	$1.03 \times 10^{40}$
50	No	$9.36 \times 10^{-4}$	$1.93 \times 10^{40}$
52	No	$1.62 \times 10^{-17}$	$3.35 \times 10^{26}$
53	1	$2.00 \times 10^{-4}$	$4.13 \times 10^{39}$
54	1	$8.44 \times 10^{-4}$	$1.74 \times 10^{40}$
57	No	$6.98 \times 10^{-14}$	$1.44 \times 10^{30}$
58	No	$5.61 \times 10^{-10}$	$1.16 \times 10^{34}$
61	No	$2.37 \times 10^{-16}$	$4.89 \times 10^{27}$
62	No	$3.27 \times 10^{-9}$	$6.75 \times 10^{34}$
66	No	$7.30 \times 10^{-12}$	$1.51 \times 10^{32}$

law of Arnett (1982) — see, for instance, Branch (1992). As can be seen in this table the amount of  $^{56}\text{Ni}$  synthesized in these simulations, and thus the corresponding luminosities, is small in almost all the cases, with a few exceptions, namely those simulations in which either the material of the lightest intervening white dwarf or of both stars is ejected as a consequence of the dynamical interaction. In particular, in those simulations in which both white dwarfs are disrupted as a consequence of a direct collision of two carbon-oxygen white dwarfs (runs 3 and 7, respectively) the masses of  $^{56}\text{Ni}$  produced during the extensive nuclear burning resulting from the interaction are of the order of  $M_{\text{Ni}} \simeq 0.7 M_{\odot}$ . Accordingly, these simulations result in Type Ia supernovae with typical luminosities ( $L \simeq 1.6 \times 10^{43} \text{ erg s}^{-1}$ ). In those runs in which the lightest white dwarf is made of helium and the direct collision results in the disruption of both stars (simulations 38, 40, and 44) the amount of synthesized nickel is

much smaller, typically of the order of  $10^{-3} M_{\odot}$ , as are the corresponding luminosities ( $L \sim 10^{40} \text{ erg s}^{-1}$ ), and would not be classified as Type Ia supernovae. When only one carbon-oxygen white dwarf is disrupted and ejected (runs 4, and 8) the masses of nickel synthesized are also considerably smaller ( $M_{\text{Ni}} \simeq 0.06 M_{\odot}$ ) and the luminosities of these events are, hence, smaller as well ( $L \sim 1.3 \times 10^{42} \text{ erg s}^{-1}$ ). Consequently, they would be classified as sub-luminous supernovae. As it occurs in those cases in which the lightest white dwarf is made of helium and both stars are disrupted, in the simulations in which only the helium white dwarf is destroyed and ejected (runs 37, 41, 42, 49, 53, and 54) the masses of nickel are very small as well. Finally, as mentioned, in the rest of the cases, namely those simulations in which the interaction does not result in the disruption of at least one star, the masses of  $^{56}\text{Ni}$  synthesized are negligible.

### 5.1 Comparison with previous works

Raskin et al. (2010) performed simulations of head-on and off-center collisions with initial parameters apparently similar to the simulations presented in this paper, and found that  $0.53 M_{\odot}$  of nickel is produced in a  $0.64 M_{\odot} + 0.81 M_{\odot}$  collision with impact parameter  $b \simeq 1.0 R_{\text{WD}}$ , whereas a negligible amount of nickel is produced in a simulation with  $b \simeq 2.0 R_{\text{WD}}$ , which results in a bound remnant. Our equivalent simulations are runs 1, 5 and 9, all of them involving two white dwarfs of masses  $0.6 M_{\odot}$  and  $0.8 M_{\odot}$ , respectively. All these simulations result in bound remnants and minuscule amounts of nickel are produced. The simulations that most closely resemble each other are our run 5, for which the distance between the centers of mass of the two stars just before the less massive white dwarf starts transferring mass to the more massive one is  $\simeq 1.9 R_{\text{WD}}$ , and simulation 2 of Raskin et al. (2010) with  $b \simeq 2.0 R_{\text{WD}}$ . In both simulations the outcome of the interaction is a bound remnant and the amount of nickel produced during the interaction is negligible. Nevertheless, to better compare with the simulations of Raskin et al. (2010) we ran a set of additional simulations. For this set of runs we adopt as a fiducial model a head-on collision of two white dwarfs of masses  $0.6 M_{\odot}$ . We emphasize that except for the masses of the colliding white dwarfs, which in our case are  $0.60 M_{\odot}$  instead of  $0.64 M_{\odot}$ , this fiducial simulation is identical to their run 1 with  $b = 0$ . For this simulation we obtain a mass of nickel of  $0.22 M_{\odot}$ , while they obtain  $0.51 M_{\odot}$ . However, we note that the amount of  $^{56}\text{Ni}$  synthesized depends very sensitively on several factors. Amongst them we mention the masses of the interacting white dwarfs, how the evolution of temperature is computed, the resolution employed in the calculations, and the adopted prescription for the artificial viscosity. We discuss them one by one.

To start with, we note that the masses of the colliding white dwarfs are slightly different in both cases and, as mentioned previously, the peak temperature reached during the interaction depends sensitively on the masses of the interacting white dwarfs, as does the mass of synthesized nickel. The second important factor to be taken into account is that the peak temperature reached during the interaction obviously depends on how the evolution of the temperature is computed. We note that for a degenerate electron gas the temperature obtained from the energy equation — see

Sect. 2 — may be incorrect by a sizable percentage. This is the reason why for those regions we adopt a different formulation and we follow the evolution of the temperature using Eq. (6), which we judge is more appropriate under these conditions. Moreover, Dan et al. (2012) have shown that the peak temperature and the averaged temperature may differ by up to a factor of  $\sim 2$  — see, for instance, their Fig. 4. Given the extreme sensitivity of the nuclear reaction rates to the temperature this, quite naturally, translates in large variations of the mass of nickel synthesized. For instance, in our fiducial simulation we obtain a peak temperature  $T_{\text{peak}} \simeq 8.21 \times 10^9 \text{ K}$ , while Rosswog et al. (2009) obtain  $T_{\text{peak}} \simeq 8.90 \times 10^9$ , which is similar to ours. However, the masses of  $^{56}\text{Ni}$  synthesized in both simulations differ considerably. In particular, we obtain  $0.22 M_{\odot}$ , whereas Rosswog et al. (2009) obtain  $0.32 M_{\odot}$ . Also the number of SPH particles plays a significant role. To quantify this we ran an additional simulation in which we decreased the number of SPH particles to  $4 \times 10^4$ , that is by a factor of 5, and we obtained that the mass of nickel synthesized in this case was  $0.094 M_{\odot}$ . Interestingly, Rosswog et al. (2009) find that when  $2 \times 10^6$  SPH particles are employed the mass of nickel synthesized in the explosion is  $0.32 M_{\odot}$ , which is quite similar to that found in our fiducial simulation, and Raskin et al. (2010) estimate that when  $5 \times 10^4$  particles are used the nickel mass should be  $\sim 0.3 M_{\odot}$  which agrees relatively well with the value found in our fiducial simulation. Moreover, Rosswog et al. (2009) find that when the Eulerian hydrodynamical code FLASH is employed in the calculations the mass of nickel is considerably smaller,  $0.16 M_{\odot}$ . Thus, our mass of nickel is bracketed by the values found by Rosswog et al. (2009). The adopted treatment of the artificial viscosity also plays a non-negligible role. To illustrate this point we also ran a series of low-resolution simulations with  $4 \times 10^4$  particles, in which the parameter  $\alpha$  in Eq. (3) was varied from 0.5 to 1.0 and 1.5. The resulting nickel masses are 0.017, 0.094, and  $0.076 M_{\odot}$ , respectively. Moreover, when the Balsara switch is not employed in the calculations the mass of  $^{56}\text{Ni}$  synthesized in the simulation with  $\alpha = 0.5$  is  $M_{\text{Ni}} \sim 0.012 M_{\odot}$ . Thus, depending on the adopted prescription of the artificial viscosity the mass of nickel can vary by up to a factor of  $\sim 5$ . In summary, we conclude that the mass of nickel synthesized depends sensitively on the details of the numerical codes, and that discrepancies of the order of a factor of up to  $\sim 3$  can quite naturally arise as a consequence of the different practical implementations of the SPH formalism.

The natural question is now why we obtain such small amounts of nickel in some of our simulations when compared with the simulations of Raskin et al. (2010)? The answer to this question lays on the choice of the initial conditions. We recall that in our simulations the initial orbits correspond to a post-capture scenario and have negative energies, whereas in the simulations of Raskin et al. (2010) the energies are positive in most cases. Hence, our orbits are always elliptical, while theirs are in most cases either parabolic or hyperbolic. This is indeed at the origin of the discrepancies in the masses of nickel found in both sets of simulations. To illustrate this point we compare our direct collision of two  $0.8 M_{\odot}$  white dwarfs (our run 6) with simulation 4 with  $b = 0$  of Raskin et al. (2010), in which two  $0.81 M_{\odot}$  white dwarfs collide head-on. We first note that the impact pa-



parameter quoted by Raskin et al. (2010) cannot be directly compared with that given by Eq. (7) because their initial orbits are open, while ours are elliptical. In our simulation we obtain a bound remnant, while Raskin et al. (2010) obtain a powerful detonation resulting in the total disruption of the system. The respective masses of  $^{56}\text{Ni}$  synthesized are in this case  $3.67 \times 10^{-3}$  and  $0.84 M_{\odot}$ . However, for these specific simulations the relative velocities between both stars at contact are very different. In particular, the relative velocities are  $v_{\text{rel}} \simeq 4.5 \times 10^3$  km/s and  $5.9 \times 10^3$  km/s, respectively. However, while in the simulation of Raskin et al. (2010) this velocity is along the line connecting the two centers of mass of the white dwarfs, in our case the velocities of each star form angles of  $\sim \pm 33.6^\circ$  with the line connecting the two centers of mass, thus resulting in a considerably less violent collision, thus in a weaker shock, and consequently in a much smaller peak temperature and in a very small mass of synthesized nickel.

## 6 CONCLUSIONS

In this paper we have studied how the interactions of white dwarfs in dense stellar systems depend on the initial conditions and on the masses of the intervening stars. Our simulations extend those of Lorén-Aguilar et al. (2010), in which the interactions of two white dwarfs of masses  $0.6$  and  $0.8 M_{\odot}$  with different initial conditions were studied, and encompass the most plausible range of white dwarf masses and internal chemical compositions. In total we have simulated 71 dynamical interactions, of which 36 correspond to runs in which a regular  $0.8 M_{\odot}$  interacts with another carbon-oxygen white dwarf (of masses  $0.6 M_{\odot}$  and  $1.0 M_{\odot}$ , respectively), and a  $1.2 M_{\odot}$  oxygen-neon white dwarf. In the rest of the simulations the dynamical interactions of a  $0.4 M_{\odot}$  helium white dwarf with either another helium white dwarf of mass  $0.2 M_{\odot}$ , or a  $0.8 M_{\odot}$  carbon-oxygen white dwarf, or a  $1.2 M_{\odot}$  oxygen-neon white dwarf were explored. Our initial conditions have been chosen to ensure that a close encounter leading to the formation of an eccentric binary or a collision always happens.

We have found that the outcome of the interactions can be a direct collision, a lateral collision or the formation of an eccentric binary system. In direct collisions there is only one violent and dramatic mass transfer episode in which the less massive white dwarf is tidally disrupted by the more massive one on a dynamical time scale, while in a lateral collision although the less massive star is disrupted as well, it takes several orbits around the more massive white dwarf to be totally destroyed. Thus, in this case the entire disruption process occurs in a more gentle way. Moreover, we have demonstrated that the outcome of the interaction can be predicted using very basic physical principles. In particular, we have found that for a given simulation tidal forces modify the initial trajectories of the interacting stars in such a way that the distance at closest approach determines the final outcome of the dynamical interaction. Specifically, we have found that if the distance at closest approach is small enough to allow a deep contact between both white dwarfs, a direct collision is the natural outcome of the interaction. For this to occur the overlap between both stars at minimum distance must be of the order of 35% if two typical carbon-oxygen

white dwarfs are considered. Else, we have demonstrated as well that lateral collisions occur when at minimum distance the radius of the less massive white dwarf is within  $\sim 0.95$  of the Roche lobe radius of the interacting system.

We have also characterized for which initial conditions of the dynamically interacting system the material flowing from the disrupted less massive white dwarf and accreted onto the more massive star is compressed to such an extent that reaches the conditions for a detonation to develop. Moreover, we have also studied for which initial conditions the explosion is powerful enough to result in the disruption of one or both of the interacting white dwarfs, and for which ones degeneracy is lifted and the result of the interaction is a central, more massive and very hot object surrounded by a debris region orbiting around it. Our results indicate that if the intervening stars are regular carbon-oxygen white dwarfs (or even oxygen-neon ones) detonations occur when the two components of the system are separated by less than  $\sim 0.015 R_{\odot}$  at minimum distance, and that one or both components of the system are totally disrupted and ejected to the surrounding medium if the total mass of the system is rather large, preferentially  $\gtrsim 1.4 M_{\odot}$  and the initial periastron distance is smaller than  $\sim 0.005 R_{\odot}$  — see Fig. 4. However, if the less massive star is a helium white dwarf the resulting detonations always result in a catastrophic output for separations at minimum distance  $\lesssim 0.02 R_{\odot}$ . Two of our simulations result in a super-Chandrasekhar Type Ia supernova outburst, corresponding to direct collisions of two rather massive carbon-oxygen white dwarfs of masses  $1.0 M_{\odot}$  and  $0.8 M_{\odot}$ . There are as well a few simulations in which only one carbon-oxygen white dwarf is disrupted and ejected. These simulations also result in powerful explosions, but their luminosities are considerably smaller and, thus, would probably be classified as sub-luminous supernovae. Finally, other simulations result in powerful outbursts, and lead as well to the disruption of the entire system, but involve white dwarfs with helium cores. In these cases the mass of  $^{56}\text{Ni}$  is very small, as are the corresponding luminosities. Nevertheless, some of our simulations produce bound remnants which are close to the Chandrasekhar limit, and the subsequent evolution of these systems may eventually produce Type Ia supernovae, as the viscous evolution unbinds only a very small fraction of the material of the debris region (Schwab et al. 2012).

For those interactions resulting in a central, massive and very hot remnant we have also studied the influence of the masses of the interacting white dwarfs and of the initial conditions on the properties of the final remnants. In particular, we have studied the morphology of the resulting remnant, the peak temperatures reached during the most violent phase of the interaction, and the associated nucleosynthesis. In all these simulations a central hot white dwarf surrounded by a debris region is formed, whereas a variable amount of mass is ejected from the system. The morphology of the debris region depends mostly on the kind of collision the system undergoes. In particular, for lateral collisions the debris region is a heavy, rotationally-supported keplerian disk, whilst for direct ones the debris regions consists of a spheroid. The peak temperatures attained during the most violent phase of the accreting episode are rather high in all cases, typically of the order of  $10^9$  K, and can be even larger for direct collisions, for which temperatures larger

than  $10^{10}$  K are easily reached, than for lateral interactions. This, in turn, drives extensive nucleosynthetic activity in the shocked regions. Hence, the debris region and the material ejected during the dynamical interaction are substantially enriched in heavy elements.

In summary, we have computed a comprehensive set of simulations aimed to provide a consistent framework to analyze the dynamical interactions of white dwarfs in dense stellar systems. These interactions are of interest because the collision is likely to detonate the white dwarfs, and result in a type Ia supernova outburst. Actually, in our simulations the detonation conditions are reached in a significant number of interactions, and the masses of the exploding systems show some dispersion. As a matter of fact, we find that for some simulations the detonation occurs in interacting systems for which the involved mass is larger than Chandrasekhar's mass, whereas in some other the resulting explosion is sub-Chandrasekhar. An important fact that needs to be taken into account is that it has been recently shown that such interactions might be more common than previously thought (Katz & Dong 2012), and could even dominate the event rate. Thus, there is a renewed interest in studying these interactions, for which there was a lack of extensive calculations. Precisely, our results fill this gap, and pave the road to more extensive calculations in which the enhancement in the event rate proposed by these authors could be analyzed in more detail. Particularly, it is worth mentioning that this increase in the event rate depends on the fraction of white dwarf collisions that are expected to lead to Type Ia-like events. Given that our calculations provide the maximum separation at pericenter for various pairs of white dwarfs to produce detonations, future calculations could approach this problem on a solid basis. Finally, another open question remains to be answered yet, namely how exactly the optical signature of the explosions resulting from these dynamical interactions would look like, even if they do not result in Type Ia supernovae. Given the wide range of nickel masses produced during the interactions studied here, they may explain both some underluminous transients and relatively bright outbursts. This is, nevertheless, out of the scope of this paper, and should be studied in future works.

## ACKNOWLEDGMENTS

This work was partially supported by MCINN grants AYA2011–23102, AYA2010–15685 and AYA2011–24780, by the AGAUR, by the European Union FEDER funds, and by the ESF EUROGENESIS project (grants EUI2009-04167 and EUI2009-04170).

## References

Arnett W. D., 1982, *ApJ*, 253, 785  
 Balsara D. S., 1995, *J. Comp. Phys.*, 121, 357  
 Barnes J., Hut P., 1986, *Nature*, 324, 446  
 Benz W., Thielemann F.-K., Hills J. G., 1989, *ApJ*, 342, 986  
 Berger L., Koester D., Napiwotzki R., Reid I. N., Zuckerman B., 2005, *A&A*, 444, 565  
 Branch D., 1992, *ApJ*, 392, 35

Charpinet S., Fontaine G., Brassard P., 2009, *Nature*, 461, 501  
 Cyburt R. H., Amthor A. M., Ferguson R., Meisel Z., 2010, *ApJS*, 189  
 Dan M., Rosswog S., Guillochon J., Ramirez-Ruiz E., 2012, *MNRAS*, 422, 2417  
 Davies M., 2002, *Roy. Soc. of London Phil. Trans. Series A*, 360, 2773  
 Eggleton P. P., 1983, *ApJ*, 268, 368  
 Fabian A. C., Pringle J. E., Rees M. J., 1975, *MNRAS*, 172, 15P  
 García-Berro E. et al., 2012, *ApJ*, 749, 25  
 Gingold R. A., Monaghan J. J., 1977, *MNRAS*, 181, 375  
 Guerrero J., García-Berro E., Isern J., 2004, *A&A*, 413, 257  
 Hawley W. P., Athanassiadou T., Timmes F. X., 2012, *ApJ*, 759, 39  
 Hernquist L., Katz N., 1989, *ApJS*, 70, 419  
 Hills J. G., Day C. A., 1976, *ApJ*, 17, 87  
 Itoh N., Totsuji H., Ichimaru S., Dewitt H. E., 1979, *ApJ*, 234, 1079  
 Katz B., Dong S., 2012, *ArXiv e-prints*  
 King A. R., Pringle J. E., Wickramasinghe D. T., 2001, *MNRAS*, 320, L45  
 Lee H. M., Ostriker J. P., 1986, *ApJ*, 310, 176  
 Lorén-Aguilar P., Guerrero J., Isern J., Lobo J. A., García-Berro E., 2005, *MNRAS*, 356, 627  
 Lorén-Aguilar P., Isern J., García-Berro E., 2009, *A&A*, 500, 1193  
 Lorén-Aguilar P., Isern J., García-Berro E., 2010, *MNRAS*, 406, 2749  
 Lucy L. B., 1977, *AJ*, 82, 1013  
 Malheiro M., Rueda J. A., Ruffini R., 2012, *PASJ*, 64, 56  
 Monaghan J. J., 1997, *J. Comp. Phys.*, 136, 298  
 Monaghan J. J., Lattanzio J. C., 1985, *A&A*, 149, 135  
 Pakmor R., Hachinger S., Röpke F. K., Hillebrandt W., 2011, *A&A*, 528, A117  
 Press W. H., Teukolsky S. A., 1977, *ApJ*, 213, 183  
 Price D. J., 2007, *PASA*, 24, 159  
 Raskin C., Scannapieco E., Rockefeller G., Fryer C., Diehl S., Timmes F., 2010, *ApJ*, 724, 111  
 Raskin C., Timmes F. X., Scannapieco E., Diehl S., Fryer C., 2009, *MNRAS*, 399, L156  
 Rosswog S., Kasen D., Guillochon J., Ramirez-Ruiz E., 2009, *ApJ*, 705, L128  
 Schwab J., Shen K. J., Quataert E., Dan M., Rosswog S., 2012, *MNRAS*, 427, 190  
 Seitenzahl I. R., Meakin C. A., Townsley D. M., Lamb D. Q., Truran J. W., 2009, *ApJ*, 696, 515  
 Serna A., Alimi J.-M., Chieze J.-P., 1996, *ApJ*, 461, 884  
 Shara M. M., Hurley J. R., 2002, *ApJ*, 571, 830  
 Shara M. M., Regev O., 1986, *ApJ*, 306, 543  
 Timmes T. X., Swesty F. D., 2000, *ApJS*, 126  
 Wagoner R. V., 1969, *ApJS*, 18, 247  
 Willems B., Kalogera V., Vecchio A., Ivanova N., Rasio F. A., Fregau J. M., Belczynski K., 2007, *ApJ*, 665, L59